

# Data Acquisition for SuperCDMS SNOLAB

by

William Alexander Page

B.A., Bowdoin College, 2013

A THESIS SUBMITTED IN PARTIAL FULFILLMENT OF  
THE REQUIREMENTS FOR THE DEGREE OF

MASTER OF SCIENCE

in

The Faculty of Graduate and Postdoctoral Studies

(Physics)

THE UNIVERSITY OF BRITISH COLUMBIA

(Vancouver)

August 2015

© William Alexander Page 2015

# Abstract

The SuperCDMS SNOLAB experiment will use solid state Germanium and Silicon detectors to search for Weakly Interacting Massive Particles (WIMPs), a leading candidate to explain dark matter. WIMPs are thought to exist in halos around galaxies and therefore thought to be constantly streaming through the earth. The CDMS detectors have been developed to measure the energy deposited by a WIMP-nucleon collision in terrestrial calorimeters.

This thesis focusses on the Data Acquisition (DAQ) system that uses Detector Control and Readout Cards (DCRCs) and is designed to be dead-time-less. The DCRCs read in the data stream from the detector's 12 phonon and 4 ionization energy channels. The DCRCs also control detector settings, and we develop interactive codes to allow users to easily change detector settings through the DCRC.

The DAQ is designed to decide which events to write to disk in order to keep data throughput under a limit yet never miss an event that will be useful in the subsequent analysis. In this effort we develop different readout methods of the detector array for the different calibration runs and WIMP search runs. We also develop fast algorithms for rejecting events that fail a certain criteria for being usable. We also present a novel data compression method that reduces the total data volume by a factor of  $\sim 16$  yet retains all important information. This method involves a large covariance matrix inversion, and we show that this inversion can be consistently computed given that a sufficient amount of data has been used to build the covariance matrix.

We also develop a GUI that is a critical element of the detector testing program for SuperCDMS SNOLAB. The GUI accesses the data stream as it is being written to disk, efficiently reads in the waveforms, and displays them in a user-friendly, oscilloscope-like, format. By making use of Fast Fourier Transform technology, the GUI is also capable of displaying incoming data in the frequency domain. This tool will enable a new degree of real-time analysis of detector performance, specifically noise characteristics, at the test facilities in the next stage of detector testing.

# Preface

The introductory chapters of this thesis (i.e. Chapters 1-3) are heavily cited to recognize the many accomplishments of others off of which a thesis such as this is based. None of the text is taken from previously published articles or internal collaboration documents.

Chapter 4 discusses software which I developed alongside my advisor, Scott Oser, and University of California Berkeley research scientist, Bruno Serfass. Chapter 5 discusses the ‘hybrid optimal filter’ method which was developed primarily by Scott Oser and myself, and sources that we found helpful are cited throughout the text.

# Table of Contents

<b>Abstract</b>	ii
<b>Preface</b>	iii
<b>Table of Contents</b>	iv
<b>List of Tables</b>	vi
<b>List of Figures</b>	viii
<b>Acknowledgements</b>	xii
<b>1 Evidence for Dark Matter</b>	1
1.1 Early Evidence	1
1.2 Galaxy Clusters	2
1.3 The Cosmic Microwave Background	4
1.4 Composition Hypotheses	5
1.4.1 The WIMP Hypothesis	6
<b>2 WIMP Detection</b>	9
2.1 Direct Detection	9
<b>3 The Cryogenic Dark Matter Search</b>	14
3.1 Semiconductor Detector Physics	14
3.1.1 Electron Recoils	15
3.1.2 Nuclear Recoils	17
3.2 Amplifiers	18
3.2.1 Measuring the $e^-/h^+$ Energy	18
3.2.2 Measuring the Phonon Energy	19
3.3 iZIP Interleaved Design	19

*Table of Contents*

---

<b>4</b>	<b>Data Acquisition</b>	22
4.1	The DCRCs	22
4.2	MIDAS and the Software Front Ends	24
4.3	The DCRC Driver	25
4.4	Detector Testing Tools	27
4.4.1	The Pulse Display	28
4.5	Readout Modes	31
<b>5</b>	<b>The Hybrid Optimal Filter</b>	33
5.1	Fourier Transform of a Hybrid Trace	35
5.2	Power Aliasing	36
5.3	Fourier Transform without the FFT	37
5.3.1	Fourier Frequencies of a Hybrid Trace	39
5.3.2	Time Points of a Hybrid Trace	40
5.3.3	The Transformation Matrix: $\mathbf{A}$	40
5.4	Determining and Inverting the Covariance Matrix	41
5.4.1	The Ratio $M/d$	43
5.4.2	Robust and Efficient Computation of the Covariance Matrix	44
5.4.3	Inversion by Choleski Decomposition	46
5.5	Time Domain Covariance Matrix and $\chi^2$	46
5.6	Amplitude and Time Offset Estimation Results	47
5.6.1	Phonon Pulse Simulation	48
5.6.2	Pulse Amplitude Resolution	49
5.7	Time Offset Resolution	51
5.8	Data Volume Consequences	51
5.9	Conclusion	53
	<b>Bibliography</b>	55
	<b>Appendices</b>	58
	<b>A The Imaginary Component of Zero and Nyquist Frequency</b>	58
	<b>B Derivation of Aliasing Frequencies</b>	60

# List of Tables

3.1	Detector specs for different generations of the Germanium CDMS detectors. Adapted from [24] and SuperCDMS SNO-LAB detector performance projections, by permission. . . .	15
5.1	Important time and frequency values for hybrid phonon waveforms. . . . .	35
5.2	Important time and frequency values for hybrid charge waveforms. . . . .	36
5.3	The baseline resolution of the HOF improves as $M/d$ increases up to $\sim 7$ . We simulated $1/f$ + white noise and 1000 phonon pulses (discussed further in sec. 5.6.1). The HOF approaches the limit of its best possible resolution, which is the resolution of the 1D uniform OF applied to the full 625kHz, 32768 point, trace. We also show the resolution by determining the covariance matrix as described in sec. 5.4.2, which shows good performance. . . . .	42
5.4	Baseline and expected resolution of different length 1D OFs and the HOF. The HOF performs as well as the 32768 point 1D OF. The uncertainty on the resolutions is $\sigma_{\sigma^2} = \sigma^2 \sqrt{\frac{2}{N-1}}$ , so $\sigma_{\sigma^2} = \sigma^2 \times 0.014$ for $N=10000$ , plus a small additional factor from the covariance matrix estimation. $1/f+wt.+ \delta$ has large noise peaks injected at 100, 1300, and 2200Hz. $1/f+wt.+ \sim$ has the normal white and $1/f$ features on top of which we add a sinusoidal in $J$ , the PSD, up to 40kHz. While the HOF seems to have superior resolution in most cases, this improvement is mostly within $1 \sigma$ uncertainty of the standard deviation, and thus assume the HOF and 32768 OF to perform equally well. . . . .	50
5.5	Time offset resolution results and the time offset's effect on the pulse amplitude estimation. The time offset estimation with 1024 points is nearly as good as with 32768 points. . .	52

*List of Tables*

---

5.6 Projected data throughput values for 42 iZIPs. A 5Hz trigger rate per detector is assumed for the Ba calibration. The live fraction is the assumed fraction of operation time spent in the specified mode. The 200TB/year and 897 TB/year values assume recomputation of the covariance matrix every 3 hours (potentially naïve). . . . . 53

# List of Figures

1.1	Rotational curves, similar to those published by Rubin, overlaid on an image of the Andromeda galaxy (M31) taken by the Palomar Sky Survey. The roughly constant velocity at high radius indicates that the high-luminosity galactic center makes up a small fraction of the total mass. (© Vera C. Rubin and Janice S. Dunlap, courtesy of Carnegie Institution DTM, by permission [3]). . . . .	2
1.2	(Left) Abell 1689 (© 2008 X-ray: NASA/CXC/MIT/E.-H Peng et al; Optical: NASA/STScI, by permission) [8]. (Right) 1E 0657-56 (© 2004 X-ray: NASA/CXC/CfA/M.Markevitch et al.; Optical: NASA/STScI; Magellan/U.Arizona/D.Clowe et al.; Lensing Map: NASA/STScI; ESO WFI; Magellan/U.Arizona/D.Clowe et al., by permission) [9] . . . . .	3
1.3	CMB power spectrum predicted by a $\Lambda$ -CDM cosmology (i.e. a dark energy (69%) and cold dark matter (26%) dominated universe). Data points in red are measurements by the Planck collaboration [11]. Power spectrum of temperature fluctuations in the Cosmic Microwave Background (© 2013 ESA/Planck, and the Planck collaboration, from Planck 2013 results. I. Overview of products and results, by permission). . . . .	5
1.4	Number density of WIMPs in the Universe as a function of time, where the relic density depends on the WIMP annihilation cross section, $\sigma_{\chi\bar{\chi}}$ or $\sigma$ in the figure. On the x-axis, $m$ is the WIMP mass while $T$ is the temperature of the universe, converted to a mass/energy by Boltzmann's constant. Evolution of a typical WIMP number density in the early universe (© NASA/IPAC Extragalactic Database (NED) which is operated by the Jet Propulsion Laboratory, California Institute of Technology, under contract with the National Aeronautics and Space Administration, by permission). . . . .	7

*List of Figures*

---

2.1	The expected WIMP event rate for the given $m_\chi$ and $\sigma_{SI} = \sigma_{\chi T}$ . $\sigma_{SI}=10^{-41}\text{cm}^2$ corresponds to roughly the cross section reported by DAMA/LIBRA, CRESST, CDMS Si, and CoGent. $\sigma_{SI}=10^{-45}\text{cm}^2$ corresponds to a cross section just below published sensitivities from 2013. Internal CDMS figure, used with permission, from [26]. . . . .	11
2.2	Current and projected limits on the WIMP mass-cross section parameter space. Figure from SuperCDMS collaboration standard public plots [29]. . . . .	13
3.1	A SuperCDMS SNOLAB iZIP 6 detector. Figure from SuperCDMS collaboration standard public plots [29]. . . . .	14
3.2	Electron stopping power in Silicon. Internal CDMS figure, used with permission, from [30]. . . . .	16
3.3	The ionization yield of different energy nuclear and electron recoil events. Ionization yield is defined as the fraction of recoil energy that goes into the $e^-/h^+$ pairs with the electron recoil ionization yield normalized to one (as seen by the horizontal lines). Internal CDMS figure, used with permission, from [24]. . . . .	17
3.4	(Left) A schematic of the CDMS II detector. The four phonon channels are colored on the top surface and the charge electrodes (Qi and Q0) are pictured on the lower surface. Figure from [37]. (Right) The iZIP design with interleaved charge electrodes ( $\pm 2V$ ) and phonon rails (0V). Internal CDMS figure, used with permission, from [34]. . . . .	20
3.5	(Left) The electric field and potential lines produced from the phonon rails (yellow) and charge electrodes (green). Notice that the unique surface E-field extends $\sim 1\text{mm}$ into the crystal and therefore surface events within this margin should exhibit asymmetric charge collection. (Right) Data from T3Z1 showing surface event discrimination (discussion in main text). Internal CDMS figure, used with permission, from [34]. . . . .	21
4.1	Cartoon showing the proposed phonon waveform readout and the ability to monitor low frequency noise. Hybrid waveform readout is discussed in chapter 5. . . . .	23

*List of Figures*

---

4.2	A Rev C DCRC. The 50-pin connector interfaces with the bias and sensor lines to the detector. The board receives power over the ethernet and also communicates with the DAQ through the ethernet port. . . . .	23
4.3	A cartoon roughly depicting the communication between the trigger front end, tower front end, the DCRC's trigger buffer, and the DCRC's circular buffer. The hypothetical data stream shows triggers labeled with yellow arrows. The time stamps of the triggers are continuously recorded in the trigger buffer and periodically read out by the trigger front end. The triggers with yellow arrows too close together would be rejected as piled-up while the other triggers would be read by the tower front end from the circular buffer. . . . .	25
4.4	(Left) Two iZIP phonon pulses that are piled-up. (Right) The rate of usable (non piled-up) events vs. the raw event rate. For this plot a 52ms long trace has been assumed (since this is the proposed data acquisition trace length), where an optimal raw rate is $\sim 20\text{Hz}$ giving a $\sim 7\text{Hz}$ usable rate. . . .	27
4.5	A screen shot of the Pulse Display displaying the PSD of two charge channels in real time. Behind the scenes, the time domain traces are grabbed from the SYSTEM buffer which are then Fourier transformed, and displayed on the screen. . .	28
4.6	A screen shot of one of the existing detector control GUIs, written primarily by A. Roberts. The detector settings (the values in red) are controlled by the user. Internal CDMS figure, used with permission. . . . .	31
5.1	Sampling scheme for phonon and charge traces. Roughly to scale. . . . .	34
5.2	Fourier coefficient spacing for phonon waveforms. . . . .	36
5.3	A PSD, using the the pasting method, of a hybrid phonon trace with certain injected frequencies. There are aliased peaks at $f=14.062\text{kHz}$ and $f = 17.186\text{kHz}$ (discussed in main text). The red line marks the folding point, $f_{Nyq,slow}$ at $19531\text{Hz}$ . . . . .	37
5.4	There are 16 frequency components in the orthogonal basis that contribute to the cosine coefficient at $\sim 9538\text{Hz}$ in the non-orthogonal basis. These frequencies match the predicted alias frequencies derived in Appendix B. . . . .	46

*List of Figures*

---

- 5.5 A phonon template, with  $A_f = 0.9, T_f = 2771\mu s, R_f = 25\mu s, F_f = 175\mu s, A_s = 0.4, T_s = 2771\mu s, R_s = 100\mu s, F_s = 816\mu s$ . The inset shows the 1024 points of fast sampled data. 48

# Acknowledgements

I am extremely thankful to my advisor Scott Oser for his supervision over these past two years. I will always be amazed by the amount of time that he is willing to invest in the education of his students. His direction and patience over my months of chipping away at the ‘hybrid optimal filter’ problem resulted in a successful conclusion (and solution), and I thank him for giving me the opportunity to take on this challenge. I am grateful for all that I have learned under his guidance.

I also owe a great thank you to Bruno Serfass, with whom I started working on Data Acquisition software, but who became an approachable source of knowledge on anything CDMS related. I am additionally indebted to Bruno for introducing me more broadly to the CDMS community, beyond the University of British Columbia group. I sincerely hope he has not wasted too much of his time in replies to my emails.

Matt Pyle has also been exceptionally generous with his time over this last summer of my M.Sc. work. It has been a privilege to learn about the CDMS detector technology from one of the foremost experts. I would also like to thank Kedar Page for meeting up with me in cafés around Vancouver to answer all the questions I had about CDMS, even though he had already completed his degree.

I also thank my family for their encouragement over these last two years.

# Chapter 1

## Evidence for Dark Matter

### 1.1 Early Evidence

In the 1920s the Dutch astronomer Jan Oort, observing the motion of stars in the Milky Way, measured the rotational speed of these stars around the galactic center. By this time, it had been determined that the bulk of the galaxy's luminous mass was at its center and this mass had been experimentally deduced. The rotational speeds of the stars found by Oort were significantly greater than those given by Newton's law of gravitation [1].

In 1933 Fritz Zwicky found the same discrepancy between expected and observed galactic rotational speeds in his observations of the Coma galaxy cluster. He computed the mass of the Coma cluster by way of the virial theorem and found it to be 400 times larger than the mass due to the luminous part alone. Zwicky called this the "missing mass" problem [2].

Since the 1930s more accurate measurements have been made of the rotation speeds of stars in our own and other galaxies. Vera Rubin pioneered the work on these measurements in her observations of the Andromeda galaxy in the 1970s. She represented her data as plots of stellar rotational speed vs. distance from galactic center, known as rotational curves, shown in fig. 1.1. Rubin is attributed with publishing the first robust evidence for dark matter and solidifying Zwicky's, Oort's, and others' earlier predictions of the existence of dark matter [3].

Newton's laws of gravitation give the rotational speed of the stars, assuming that all matter in the galaxy is luminous and roughly estimated to be concentrated at the center, as:

$$v(r) = \sqrt{GM} \sqrt{\frac{1}{r}}.$$

From Rubin and other more recent measurements (e.g. [4]) we know that the rotation speed of stars does not fall off as  $r^{-1/2}$ . Rather speeds are roughly constant at large radius from the galactic center, suggesting that luminous matter makes up only a small portion of the total mass and that non-luminous "dark" matter is distributed around the galaxy.

## 1.2. Galaxy Clusters

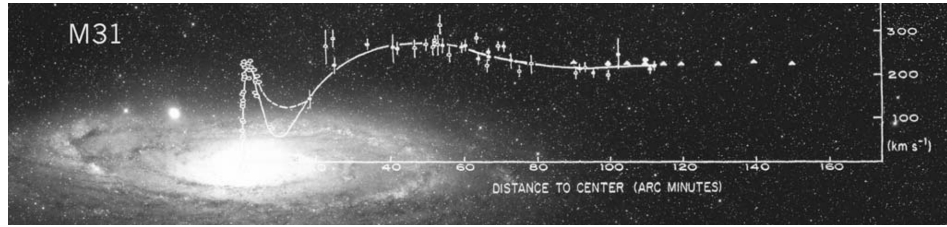


Figure 1.1: Rotational curves, similar to those published by Rubin, overlaid on an image of the Andromeda galaxy (M31) taken by the Palomar Sky Survey. The roughly constant velocity at high radius indicates that the high-luminosity galactic center makes up a small fraction of the total mass. (© Vera C. Rubin and Janice S. Dunlap, courtesy of Carnegie Institution DTM, by permission [3]).

If we instead modeled mass in the galaxy as a spherically symmetric distribution that varies with distance,  $M(r)$ , the constant stellar rotational velocity at large distances given by  $v = C = \sqrt{GM(r)}\sqrt{\frac{1}{r}}$ , can be explained by an enclosed mass that varies linearly with the distance from the center:

$$M(r) \propto r.$$

Therefore the enclosed mass has a density proportional to the inverse square of the distance from the galactic center,  $\rho(r) \propto \frac{1}{r^2}$ . Most of this matter must be dark because the luminous mass density falls off much more rapidly. To account for this missing matter, the leading model is a spherically symmetric “halo” of dark matter distributed throughout our galaxy and other galaxies, interacting gravitationally and making up the majority of mass in the galaxy and the universe.

## 1.2 Galaxy Clusters

Measurements of galaxy clusters since Zwicky have provided additional evidence for dark matter and important information regarding the composition of dark matter. Observations of galaxy clusters—the largest gravitationally collapsed astrophysical structures—are particularly powerful because different techniques can be used to make independent measurements of their mass.

The Chandra Observatory measures the x-ray emission from the intergalactic gas of galaxy clusters. With the clusters’ gravitational potential

## 1.2. Galaxy Clusters

---

largely due to dark matter, their intergalactic gas gains kinetic energy and heats to  $\sim 10^8\text{K}$ , and they are therefore among the brightest x-ray sources [6]. By measuring the x-rays, the temperature and pressure of the gas can be computed. If the cluster is in equilibrium (which excludes merging or colliding clusters), the gravitational potential can be computed under the good assumption that gravitational forces cancel with pressure forces. Recent publications matching models of the interstellar gas and dark matter halo to Chandra Observatory data indicate that ordinary matter makes up 12-15% of the total mass of the cluster [6] [7]. Figure 1.2 (left) shows Abell 1689, the largest known galaxy cluster which contains  $\sim 1000$  galaxies. The intergalactic gas, emitting in the the x-ray, is shown in purple. The optical image is overlaid and shows some distortion and arcing of luminous background objects characteristic of strong gravitational lensing.

In an independent measurement of the cluster mass, the Hubble Space Telescope measures light from background objects that bends around the massive structures. The total gravitational mass of the cluster is computed by the strength of the gravitational lensing, which confirms that the majority of gravitational mass of the clusters is not due to the luminous matter[5].

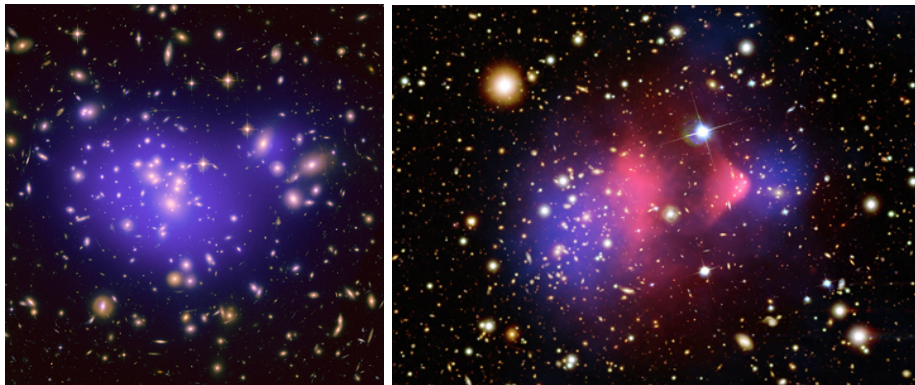


Figure 1.2: (Left) Abell 1689 ( $\copyright$  2008 X-ray: NASA/CXC/MIT/E.-H Peng et al; Optical: NASA/STScI, by permission) [8]. (Right) 1E 0657-56 ( $\copyright$  2004 X-ray: NASA/CXC/CfA/M.Markevitch et al.; Optical: NASA/STScI; Magellan/U.Arizona/D.Clowe et al.; Lensing Map: NASA/STScI; ESO WFI; Magellan/U.Arizona/D.Clowe et al., by permission) [9] .

The “Bullet” Cluster is one of the most famous examples of the dark matter making itself apparent in our universe. The Hubble Space Telescope and Chandra Observatory have observed the collision of two galaxy clus-

ters and measured the distributions of both the gravitational matter from strong gravitational lensing and luminous matter from x-ray emission. As shown in figure 1.2 (right), these two distributions are observed to have separated. The luminous matter (pink) is superimposed on the distribution of gravitational matter (i.e. predominantly dark matter) as measured by lensing (purple). The two dark matter distributions have passed through each other while the luminous distributions lag behind due to the impedance of their collisions. The nearly non-interacting dark matter streams through unimpeded.

### 1.3 The Cosmic Microwave Background

If we follow this chapter's progression to physically larger scales, from the individual galaxies of section 1.1 to the galaxy clusters of section 1.2, then the Cosmic Microwave Background (CMB) is certainly the next topic to discuss. Approximately 400,000 years after the Big Bang, the expanding universe cooled to a point where it became energetically favorable for the plasma of protons and electrons to fall out of equilibrium with photons and form neutral hydrogen. At this point of 'recombination,' the universe became transparent to the photons which make up the CMB radiation, which matches a blackbody spectrum with (currently) a temperature of 2.7K. Slight differences, or anisotropies, in this temperature across the sky, on the order of  $10\mu\text{K}$ , have been a rich source of cosmological information, including the most accurate measure of the non-baryonic (dark matter) matter density in the universe.

Transforming the spacial anisotropies into spherical harmonics (and taking the magnitude) gives the CMB power spectrum. The acoustic peaks of the power spectrum show the angular scales at which the photons were slightly hotter and denser than average at recombination (and today). The hotter overdensities are well understood as regions where the photons, coupled to the baryonic matter right up to the point of recombination, had clumped together because of gravitational wells into which the baryonic matter were attracted.

Most importantly for the case of non-baryonic dark matter, the size of the peaks would be much smaller if these gravitational wells had been formed by baryonic matter alone. This is because the pressure of the photons coupled to the baryonic matter opposes the formation of gravitational wells. In order to accurately model the location and size of the peaks, a decoupled non-baryonic matter component must exist which continues to collapse regardless

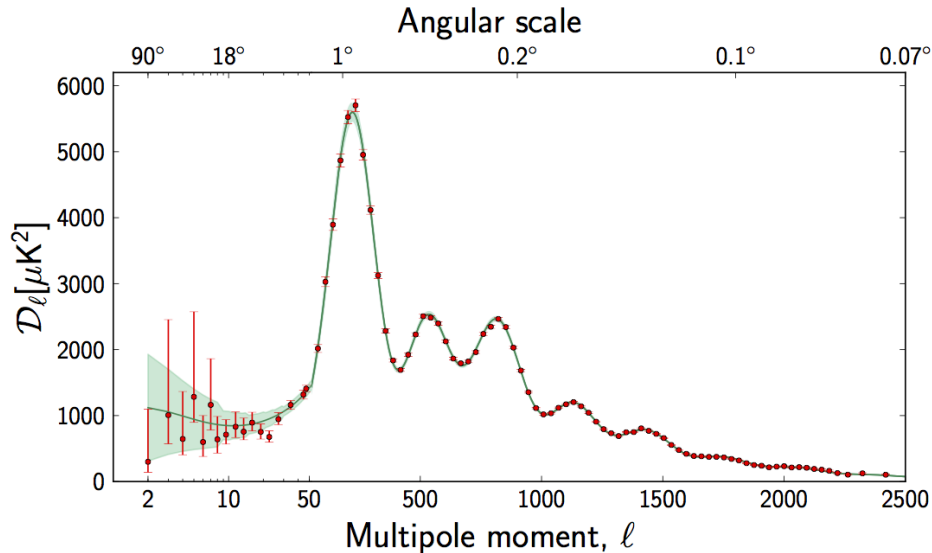


Figure 1.3: CMB power spectrum predicted by a  $\Lambda$ -CDM cosmology (i.e. a dark energy (69%) and cold dark matter (26%) dominated universe). Data points in red are measurements by the Planck collaboration [11]. Power spectrum of temperature fluctuations in the Cosmic Microwave Background (© 2013 ESA/Planck, and the Planck collaboration, from Planck 2013 results. I. Overview of products and results, by permission).

of the photon restoring force. The photon pressure restoring force does set up an oscillation of the baryon-photon plasma, which is highly sensitive to the non-baryonic matter density, and which is imprinted on the CMB at last scattering in the form of the peaks in the power spectrum [13].

While the baryonic and non-baryonic matter densities are degenerate with other cosmological parameters in determining the location and size of the peaks, the degeneracies can be broken by including other cosmological data (e.g. 21cm and supernovae measurements). The best current measurement of the cold dark matter density fraction of the universe is 26% (with a 69% dark energy component) [11].

## 1.4 Composition Hypotheses

Despite overwhelming observational evidence that dark matter does exist, very little is known about its composition. A number of theories have been

put forth.

In one effort to account for the dark matter, collaborations searched for hidden massive compact halo objects (MACHOs), such as black holes or massive non-luminous planets. They looked for MACHOs in the Milky Way by waiting for slight unexpected gravitational lensing of distant luminous galaxies as a MACHO passed between us and the galaxy. These searches ruled out the possibility of MACHOs constituting any more than 25% of the Milky Way’s dark matter halo, and therefore disqualified them as the primary dark matter candidate [10].

Most theories predict that non-baryonic particles make up dark matter halos around galaxies, but still there exist many possibilities for the type of particle. If we assume that dark matter is non-baryonic, it is highly likely that such dark matter is also non-relativistic, or “cold”, dark matter. Relativistic, or “hot,” dark matter conflicts with the accepted model of galaxy formation [14]. Returning to the discussion of section 1.3, had the dark matter been relativistic then its kinetic energy would have largely prevented its gravitational collapse. However, the gravitational landscape at recombination is well understood, and not only is it imprinted on the CMB but it also explains the formation of the dense small scale structures (galaxies) seen in the universe today. That the majority of dark matter is cold rules out a hot relativistic (neutrino-like) species from contributing substantially to the 26% dark matter component.

With these requirements, Axions and WIMPs are the two leading dark matter candidates. The axion particle was originally proposed as a solution to the strong CP problem [15] and has since become an leading ultra-light mass (100keV to 1MeV) dark matter candidate. The ADMX experiment searches for axions by detecting axion-to-photon conversion in a strong magnetic field resonance cavity [16].

The SuperCDMS experiment, along with many competitor experiments, searches for WIMPs. We will devote the remainder of this chapter and chapter 2 to discussion of this hypothetical particle.

### 1.4.1 The WIMP Hypothesis

The WIMP hypothesis is intriguing because it fits into a parameter space supported by supersymmetric (SUSY) theory as well as cosmology. By satisfying the above cosmological constraints, it is likely that WIMPs are a thermal relic of the Big Bang phase of the universe, that “froze out” of the primordial plasma at early times. The dark matter density at freeze out (and today) is highly sensitive to the the WIMP cross section  $\sigma_{\chi\bar{\chi}}$ . For

#### 1.4. Composition Hypotheses

WIMPs to make up the 26% energy density of the universe, the WIMP cross section must be on the scale of the weak force where SUSY postulates that new particles could exist.

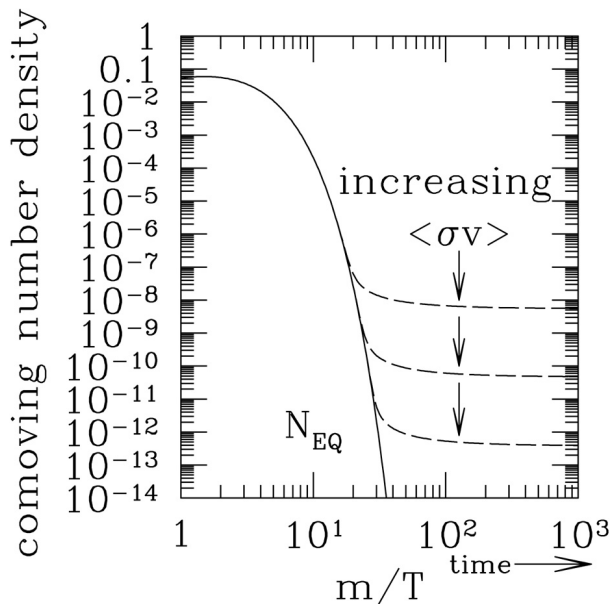


Figure 1.4: Number density of WIMPs in the Universe as a function of time, where the relic density depends on the WIMP annihilation cross section,  $\sigma_{\chi\bar{\chi}}$  or  $\sigma$  in the figure. On the x-axis,  $m$  is the WIMP mass while  $T$  is the temperature of the universe, converted to a mass/energy by Boltzmann's constant. Evolution of a typical WIMP number density in the early universe (© NASA/IPAC Extragalactic Database (NED) which is operated by the Jet Propulsion Laboratory, California Institute of Technology, under contract with the National Aeronautics and Space Administration, by permission).

A number of assumptions regarding matter in the early universe allows cosmologists to estimate the WIMP cross section and mass. First, WIMPs would have been in constant creation and annihilation until some critical point of the universe's cooling where the low temperature would prevent any further WIMP creation. Following this, expansion of the universe would have made it exponentially unlikely that a WIMP would collide with its antiparticle and annihilate [18]. This second critical moment—when annihilation ceases—determines particle abundance and depends on the WIMP

#### 1.4. *Composition Hypotheses*

---

annihilation cross section as shown in Fig. 1.4. In order to account for the dark matter in the universe, the WIMP annihilation cross section is estimated to be roughly at the scale of the weak force where yet undiscovered particles are expected to exist [19] .

This coincidence is what some refer to as the “WIMP miracle.” SUSY was proposed in order to solve the hierarchy problem (the large discrepancy between the magnitude of the weak force and the gravitational force) and SUSY could provide elegant means of unifying gravity with the other three fundamental forces [19]. SUSY adds particles to the Standard Model and the lightest of these particles, the neutralino, could be exactly what experimentalists are looking for in the WIMP. The Minimal Supersymmetric Standard Model places the neutralino mass less than the TeV scale [19]. This convergence of SUSY and cosmology is the primary motivation behind the WIMP hypothesis and has launched the dozens of experiments attempting to detect WIMPs [19].

## Chapter 2

# WIMP Detection

The WIMP dark matter detection effort is sufficiently large that this thesis will not attempt to review the field of experiments pushing to make the first credible WIMP discovery. Here we quickly mention the leading searches that are constraining dark matter parameters and excluding certain models.

Experimentalists at the LHC attempt to create dark matter through particle collisions, and to observe an absence of energy in their detector as the dark matter particle passes through [20]. Telescopes on earth and aboard satellites seek to observe excess gamma ray signals in nearby dwarf galaxies as a signature of dark matter annihilation in the dense galactic center [21]. Experiments like Super-Kamiokande and IceCube search for dark matter annihilation through the neutrinos they produce [22].

Direct detection experiments look for WIMP-nucleon recoils in terrestrial detectors and employ different targets (e.g. liquid argon, liquid xenon, germanium, silicon, calcium tungstate), background rejection techniques, amplifiers, and/or energy thresholds. Direct detection experiments are optimized (or equivalently, limited) to certain WIMP masses and cross sections based on their detector technology.

### 2.1 Direct Detection

In order to measure the energy deposited by a WIMP-nucleon collision, detectors must be capable of measuring energies on the order of 1keV. The (purely classical) expected energy transfer to a target in a WIMP collision is given by:

$$E_{recoil} = \left(\frac{m_\chi m_T}{m_\chi + m_T}\right)^2 \frac{v^2}{m_T} (1 - \cos(\theta_\chi)) \quad (2.1)$$

where  $m_\chi$  is the WIMP mass,  $m_T$  is the target mass,  $v$  is the WIMP velocity, and  $\theta_\chi$  is the WIMP scattering angle.

The WIMP velocity is given by  $v$  and deserves brief discussion. In the Standard Halo Model (SHM) the dark matter halo is overall stationary with

## 2.1. Direct Detection

---

respect to the galaxy, and therefore the local WIMP velocity is given approximately by the Sun’s rotational velocity ( $v \approx 220 \text{ km/s} \approx 7 \times 10^{-4} c$ ). It is standard to model statistical fluctuations in the WIMP velocity, in the galactic rest frame (where the bulk WIMP velocity is zero), by a Maxwellian distribution [25]:

$$f(v) = \begin{cases} A e^{(-v^2/v_0^2)} & v < v_{esc} \\ 0 & v > v_{esc} \end{cases} \quad (2.2)$$

where  $v_0 = 7 \times 10^{-4} c$  and  $v_{esc}$  is the local escape velocity ( $v_{esc} \approx 4.5 \times 10^{-3} c$ ).

One key element of direct detection is made clear from equation 2.1—the WIMP cannot efficiently transfer energy to target components that are much less massive than a nucleon. Consider the maximum energy transfer of a WIMP-electron collision ( $\theta_\chi \rightarrow 180^\circ$ ,  $m_T \approx m_e$ ), giving  $E_{recoil} \approx 2m_e v^2 = 0.25 \text{ eV}$ . Signals of this magnitude will be entirely buried under the noise floor of detectors for even the lowest threshold next generation dark matter experiments (SuperCDMS SNOLAB HV detector thresholds will be on the order of 100eV).

Instead consider the maximum energy transfer of a WIMP-nucleon collision where the dark matter particle is well matched kinematically to a Ge nucleus target: ( $\theta_\chi \rightarrow 180^\circ$ ,  $m_\chi \approx m_T \approx 72m_p$ ). In this case  $E_{recoil} \approx (1/2)m_T v^2 \approx 16.5 \text{ keV}$ , which is certainly an energy capable of detection.

Next, since the local dark matter density is approximately  $0.3 \text{ GeV/cm}^3$  (i.e. many WIMPs streaming through the detectors every day), direct detection experiments hope to measure this steady rate of WIMP events. The expected differential scattering rate, which of course depends on  $E_{recoil}$ , is given by:

$$\frac{dR}{dE_{recoil}} = \frac{\rho}{m_T m_\chi} \int_{v_{min}}^{\infty} v f(v) \left[ \frac{d\sigma_{\chi T}}{dE_{recoil}}(v, E_{recoil}) \right] dv \text{ [keV kg day]}^{-1} \quad (2.3)$$

where  $d\sigma_{\chi T}/dE_{recoil}$  is the differential cross section and  $v_{min}$  is the minimum WIMP velocity in order to produce recoil energy  $E_{recoil}$ .<sup>1</sup>

Except for the differential cross section  $d\sigma_{\chi T}/dE_{recoil}$  and the WIMP mass, all the parameters of the differential scattering rate are estimated in the SHM. The differential cross section, while largely unknown, clearly has large implications on the detectability of WIMP particles. The total

---

<sup>1</sup>The rotation of the earth around the sun seasonally adds and subtracts from the WIMP velocity relative to the earth and detecting a seasonal variation in a possible WIMP signal would be another sign that the signal is indeed the dark matter halo. A different direct detection experiment—the DAMA/LIBRA collaboration—claims that they are seeing this annual modulation in their data [27].

## 2.1. Direct Detection

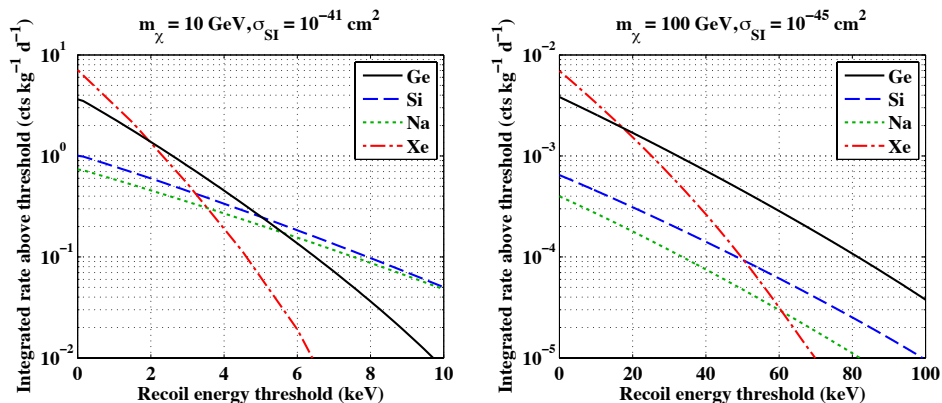


Figure 2.1: The expected WIMP event rate for the given  $m_\chi$  and  $\sigma_{SI} = \sigma_{\chi T}$ .  $\sigma_{SI}=10^{-41}\text{cm}^2$  corresponds to roughly the cross section reported by DAMA/LIBRA, CRESST, CDMS Si, and CoGent.  $\sigma_{SI}=10^{-45}\text{cm}^2$  corresponds to a cross section just below published sensitivities from 2013. Internal CDMS figure, used with permission, from [26].

cross section could be the sum of a spin independent and spin dependent term, although the spin independent term is expected to be amplified. As Witten and Goodman noted in their 1978 paper [23], the spin independent term in the cross section scales as the number of nucleons ( $A$ ) squared, which greatly increases the likelihood and conceivability of a direct WIMP detection.  $A^2$  scaling is due to the low-momentum WIMP-nucleon collisions, which does not probe the nuclear structure, which leads to coherent adding of the scattering amplitudes. Even so, lower bounds on the WIMP cross section of most models extend below the coherent neutrino scattering limit shown on figure 2.2. The solar and atmospheric neutrinos to which detectors become sensitive below these WIMP cross sections present a serious obstacle for beyond-next-generation direct detection experiments.

More optimistically, D. Moore computed the integral in equation 2.3 for different targets and different cross sections (figure 2.1). In the (overly optimistic) left plot he used a cross section from disputed WIMP detection claims and in the right plot he used cross sections just below the current published sensitivities. As a rough reference, reading off from figure 2.1 (left), a recoil threshold of 6keV gives a rate of  $1/10$  [events  $\text{kg}^{-1}\text{day}^{-1}$ ]. CDMS II had roughly 5kg of detector bulk (Ge and Si), translating to a rate of 0.5 events per day.

At these relatively low nuclear-recoil energies and low event-rates, one fundamental challenge to direct detection experiments is background dis-

## 2.1. Direct Detection

---

crimination. One advantage is that the majority of backgrounds will scatter off electrons in the detector bulk. All competitive (with the exception of CDMS HV detectors) direct detection technologies have means to distinguish electron recoils from nuclear recoils and thus reject background events. CDMS's background discrimination technique will be discussed in more detail in chapter 3.

The above is *in principle* how CDMS and other direct detection experiments intend to discover WIMPs and measure  $\sigma_{\chi T}$  and  $m_\chi$ . However, ever since 2002 when the first generation of CDMS results were published, no such rate (that has been widely accepted within the community) has been observed. CDMS has gone through three generations of experiments: CDMS, CDMS II, SuperCDMS Soudan, and is now preparing for SuperCDMS SNOLAB. Each generation of the experiment has increased the total detector mass and implemented improved detector technology. In two of the iterations the detectors were moved to a cosmogenically cleaner (deeper) and radiogenically cleaner site. Meanwhile competitor experiments made similar improvements and new detection technologies were developed, all in order to combat the two primary difficulties facing WIMP direct detection: (1) a low rate of WIMP-nucleon collision, and (2) background rejection.

## 2.1. Direct Detection

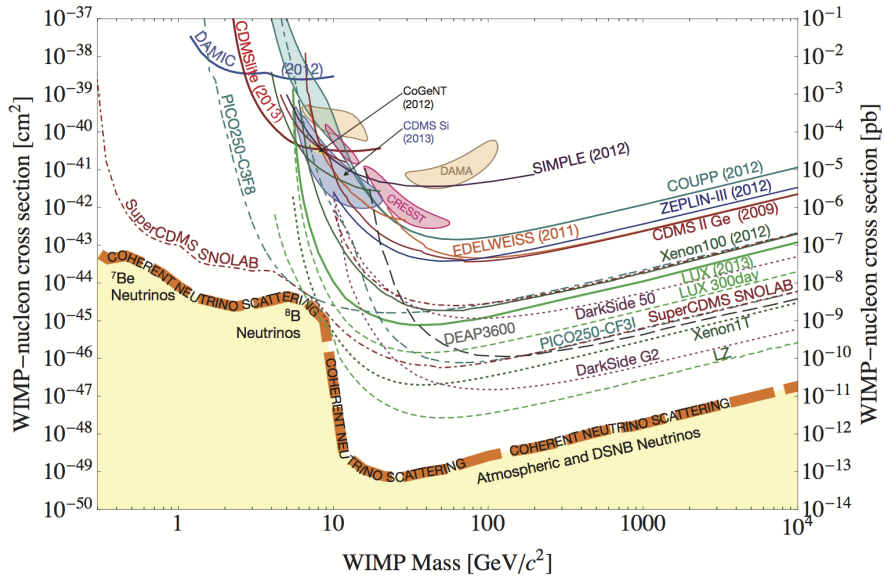


Figure 2.2: Current and projected limits on the WIMP mass-cross section parameter space. Figure from SuperCDMS collaboration standard public plots [29].

## Chapter 3

# The Cryogenic Dark Matter Search

### 3.1 Semiconductor Detector Physics

The CDMS detector bulk is ultra pure crystalline germanium and silicon. The response of cryogenically cooled crystalline semiconductors to a nuclear recoil versus an electron recoil provides CDMS with the ability to discriminate between a potential WIMP signal and background events. Additionally, the availability of radioactively stable Ge and Si, free of radioactive contaminants, ensures that any energy deposited in the crystal is the result of a foreign particle collision. Si and Ge also have good charge transport properties and small band gaps [28], the importance of which will be elaborated on in section 3.1.1.

As shown in Table 3.1, the mass of each individual detector is on the order of one kg and they are about the size of a hockey puck (fig. 3.1). The detectors are stacked in towers, each of which (for SuperCDMS SNOLAB) holds 6 detectors.

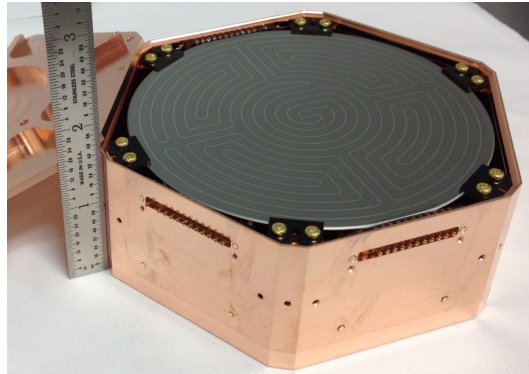


Figure 3.1: A SuperCDMS SNOLAB iZIP 6 detector. Figure from SuperCDMS collaboration standard public plots [29].

### 3.1. Semiconductor Detector Physics

	<b>CDMS II</b>	<b>SCDMS Soudan</b>	<b>SCDMS SNOLAB</b>
Detector	ZIP	iZIP	iZIP (HV)
Mass per Detector [kg]	0.25	0.62	1.38 (1.38)
Number of Detectors	19	15	~42 (~6)
Total Ge Mass [kg]	4.75	8.89	~58 (~8)
Phonon Channels per Det.	4	8	12 (~16)
Phonon Energy Res. [eV]	180	200	~75 (~50)
Trigger Threshold [eV]	~2000	~3000	~550 (~350)
Charge Energy Res. [eV]	300	450	~200 (-)

Table 3.1: Detector specs for different generations of the Germanium CDMS detectors. Adapted from [24] and SuperCDMS SNOLAB detector performance projections, by permission.

Ever since 2003, CDMS has been operating out of the Soudan mine (~2300ft below surface) in Minnesota and the SuperCDMS SNOLAB experiment is scheduled to start taking data in the SNOLAB facility (~6800ft below surface) in 2018. The earth above these facilities serves as a shield of cosmic ray muons.

Additional shielding is added locally around the detectors. The towers sit in a muon veto cage in the event that a cosmic ray muon does penetrate into the facility. Ancient, non-radioactive, lead surrounds the detectors and serves to absorb gamma rays while a polyethylene cover is in place to absorb neutrons. A copper enclosure shields from alpha and beta radiation.

Because any particle (WIMP or background) that interacts within the detector does so in (1) an electron recoil or (2) a nuclear recoil, we now discuss the basic physics of these interactions and why they form the basis of the detectors' sensitivity to WIMPs. The ideas behind this discussion of nuclear vs. electron recoils in semiconductors come from Jan Lindhard's work, published in the 1960's, which is known as Lindhard theory [31].

#### 3.1.1 Electron Recoils

Most background particles ( $\alpha, \beta, \gamma$ ) are far more likely to recoil off electrons in the detector bulk. For example, when a medium energy  $\gamma$ -ray (10keV to 1MeV) passes through the detector bulk, it is likely to Compton scatter and create electron-hole ( $e^-/h^+$ ) pairs along its track[37]. In germanium, where the energy to create an  $e^-/h^+$  pair ( $E_{create}$ ) is 2.96eV, a 10keV  $\gamma$  produces 3000  $e^-/h^+$  pairs under the good assumption that it is fully

### 3.1. Semiconductor Detector Physics

absorbed. Similarly,  $\alpha$  and  $\beta$  background recoil off electrons and ionize  $e^-/h^+$  pairs in equal proportions to their energy.

A recoiling electron will lose energy by transferring it to other surrounding electrons. Fig. 3.2 gives the stopping power for recoiling electrons in Si (which is similar to that in Ge). Note that on this plot the x and y energy scales are comparable, and the y axis gives the energy loss per  $\mu\text{m}$ . Equivalently, all but the highest energy ( $> 10^5\text{eV}$ ) recoiling electrons only travel at maximum a matter of  $\mu\text{m}$  before losing most of their energy. We can be confident in the assumption that all of a recoiling electron's energy will be deposited within the crystal.

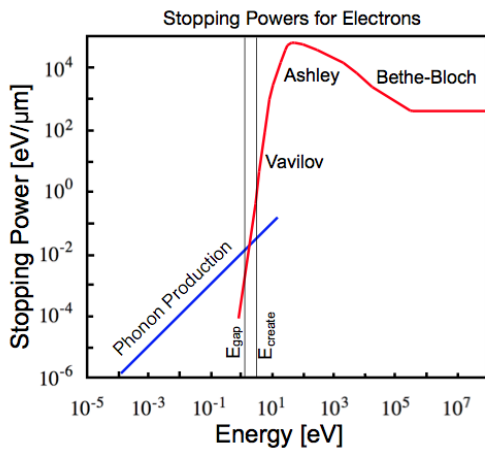


Figure 3.2: Electron stopping power in Silicon. Internal CDMS figure, used with permission, from [30].

How does the recoiling electron lose its energy to other electrons? An electron with sufficient energy to create another  $e^-/h^+$  pair ( $E_{create}$ ) will do so until its energy falls below  $E_{create}$ . The newly ionized electrons will similarly ionize other  $e^-/h^+$  pairs, creating an electron cascade. Energy is distributed to other local electrons until every electron's energy is below  $E_{create}$ . At this point, the electrons are still capable of losing energy, but no longer by ionization. Instead they transfer their energy to vibrations in the crystal lattice (phonons), which then travel like particles through the crystal [24]. Electrons radiate in this manner until they reach the gap energy ( $E_{gap}$ ) of the material, which is the minimum energy that an excited electron can have. Therefore, an electron recoil results in two types of energy deposited in the crystal:  $e^-/h^+$  pair energy and phonon energy.

We can roughly calculate the expected energies channeled into  $e^-/h^+$  pair and phonon production. Given some initial electron recoil energy, the fractional charge energy is given by  $E_{gap}/E_{create}$  and the fractional phonon energy given by  $1 - E_{gap}/E_{create}$ . In germanium, where  $E_{gap}=0.785\text{eV}$  and  $E_{create}=2.96\text{eV}$ , roughly 25% of electron recoil energy goes into  $e^-/h^+$  pairs[24].

### 3.1.2 Nuclear Recoils

WIMPs and neutrons (a particularly toxic background) recoil off Ge and Si nuclei in the CDMS detector bulk. Nuclear recoils are similar to electron recoils in many ways; however, they differ most importantly in that a lower fraction of energy goes into  $e^-/h^+$  pairs than in electron recoils.

When a nucleus recoils, it is capable of transferring energy to other nuclei *and* other surrounding electrons. Nuclei are capable of this from a purely kinematic standpoint, whereas electrons are not because of their small mass [31]. Let us consider a high energy nuclear recoil and a low energy nuclear recoil separately in order to discuss how energy is partitioned. In a high energy nuclear recoil ( $\sim 1\text{MeV}$  in Ge), most of the energy goes into the electron cascade (figure 3.3) [31]. Therefore, a high energy nuclear recoil looks a lot like an electron recoil in the detectors.

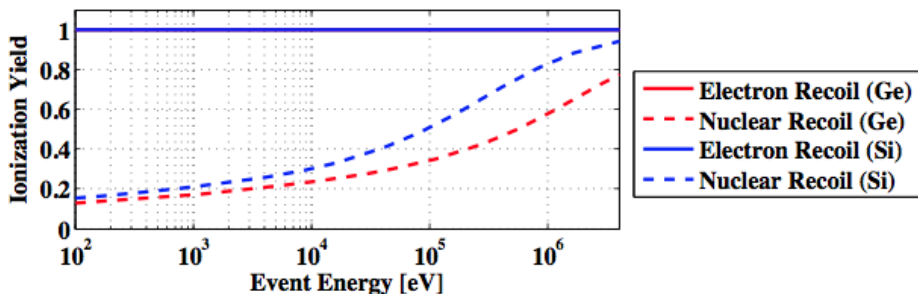


Figure 3.3: The ionization yield of different energy nuclear and electron recoil events. Ionization yield is defined as the fraction of recoil energy that goes into the  $e^-/h^+$  pairs with the electron recoil ionization yield normalized to one (as seen by the horizontal lines). Internal CDMS figure, used with permission, from [24].

A lower energy nuclear recoil, however, transfers energy more evenly between excitations of electrons and excitations of other nuclei [31]. The

nuclei are freed from the crystal lattice and excite other nuclei in a cascade separate from the electron cascade. Once the nuclei have insufficient energy to excite another nuclei they lose their energy to phonon production. This time, however, there is no analogous  $E_{gap}$  for phonons as there was in the electron case. Therefore, nuclear cascades are more efficient than electron cascades in the final phonon production[31]. Figure 3.3 displays this aspect of nuclear recoils over a range of recoil energy.

From the discussion of section 2.1, clearly it is the lower energy ( $<500\text{keV}$ ) nuclear recoils that are expected from WIMPs. The event discrimination in this energy range provides the CDMS detectors with their sensitivity to WIMPs masses above  $5\text{GeV}$ .

## 3.2 Amplifiers

The detector surfaces are instrumented with sensors designed to measure the  $e^-/h^+$  and phonon energy with optimal resolution. As resolutions improve, event discrimination improves and (perhaps more importantly) detector thresholds can be lowered.

### 3.2.1 Measuring the $e^-/h^+$ Energy

Once an electron cascade has occurred, the detectors prevent the excited  $e^-/h^+$  pairs from de-exciting back into valence states by applying a voltage across the detector. The electric field drifts the charges to the flat detector endcaps. In standard CDMS iZIP detectors, the voltage has been tuned to the smallest value such that charge trapping in crystal impurities is also minimized. The optimal field is  $\sim 1\text{V/cm}$ . In SuperCDMS iZIP detectors, FET (Field Effect Transistor) amplifiers read out the image charge on the electrodes and amplify this signal as a voltage that is read out and further amplified by downstream amplifiers. Because the fall time of the SuperCDMS iZIP amplifier is larger than the charge collection time ( $\sim 1\mu\text{s}$ ), a voltage pulse proportional to the charge collected is the only information that is obtained from the charge amplifier [37]. SuperCDMS SNOLAB will use HEMTs (High Electron Mobility Transistors) in place of FETs, primarily to reduce heat load on the fridge, but which rely on the same basic amplification principles described above.

### 3.2.2 Measuring the Phonon Energy

Six phonon channels are implemented on each detector surface, and each channel consists of thousands of Transition Edge Sensors (TESs). The TESs are made from Tungsten superconducting material whose transition temperatures ( $T_c$ ) are tuned in fabrication to be anywhere between 30mK and 200mK. The voltage biased TESs are held within the range of their transition such that when heat from phonons reach the sensors their resistance changes rapidly and the current through them drops. The current through the TES is inductively coupled to a SQUID which further amplifies the reduction in current. TESs, which are at the heart of the CDMS detectors' sensitivity to dark matter, have also propelled the fields of x-ray astronomy and CMB cosmology to their current states, and the sensor technology is reviewed in K. Irwin's and G. Hilton's seminal chapter [32].

Unlike the charge measurement, more than just the phonon energy is encoded in the phonon measurement. We obtain an estimate of the event location by comparing the energy deposited in the different phonon channels. We have a good idea for how phonons move through the crystalline bulk because the anisotropic and incoherent propagation of phonons in crystalline semiconductors is well modeled by CDMS's detector Monte Carlo [33]. Therefore the partitioning of energy in the different channels allows a weighted average of sorts to determine the x and y coordinate of the initial event[37]. The pulse shape of the phonon energy signal is also occasionally used to obtain more information about the event.

## 3.3 *iZIP Interleaved Design*

While the CDMS II ZIP detectors were beautiful devices with world-leading WIMP sensitivity in their time, they suffered primarily from one design flaw. The ionization from electron recoils close to the detector surface was more prone to trapping which reduced the ionization yield of the event [34]. This reduced ionization yield caused surface electron recoils to mimic the nuclear recoil signature and thus leak into the WIMP signal region. CDMS II sensitivities were limited by this background [34].

A new detector (the *iZIP*) was designed to provide a solution to discriminate the surface event background. The ionization electrodes are interleaved between the phonon sensors which allows readout of both ionization and phonon energy on each detector face. Just as importantly, the phonon TES rails are maintained at 0V while the ionization electrodes are kept at opposite potentials ( $\pm 2V$  in standard operation) on either face. This configura-

### 3.3. *iZIP Interleaved Design*

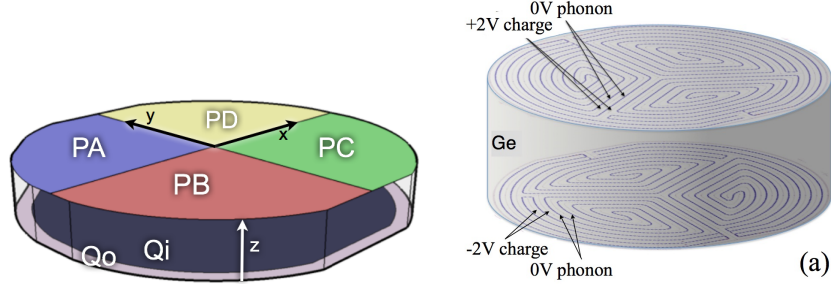


Figure 3.4: (Left) A schematic of the CDMS II detector. The four phonon channels are colored on the top surface and the charge electrodes ( $Q_i$  and  $Q_0$ ) are pictured on the lower surface. Figure from [37]. (Right) The *iZIP* design with interleaved charge electrodes ( $\pm 2V$ ) and phonon rails ( $0V$ ). Internal CDMS figure, used with permission, from [34].

tion produces a unique electric field within the crystal (figure 3.5) wherein the ionization from surface events will largely be collected on one side of the detector face. The CDMS and EDELWEISS collaborations have shown that the interleaved design allows for robust rejection of surface events. An analysis cut on asymmetric charge collection on side 1 vs. side 2 of the *iZIP* rejects the surface events.

Figure 3.5 (right) shows the ionization yield vs. recoil energy for events from 900 hours of exposure of Soudan *iZIP* T3Z1 to a  $^{210}\text{Pb}$  source. The  $^{210}\text{Pb}$  source was found, as expected, to produce  $\sim 130$  surface electron recoils per hour via beta decay. These events exhibit reduced ionization yield and fail the symmetric charge cut. They populate the region above the  $2\sigma$  nuclear recoil band and below ionization yields of  $\sim 1$ . The events below the germanium nuclear recoil band but also failing the symmetric charge cut are surface events from recoiling  $^{206}\text{Pb}$  nuclei (the end product of the  $^{210}\text{Pb}$  decay). The colored blue dots are events that pass the symmetric charge charge and accordingly show large ionization yield corresponding to bulk electron recoils. Out of the 90,000 events in this plot, two outliers exist which (barely) pass the charge symmetry cut but show low ionization yield, which are blue and circled in black [34]. Overall, this study demonstrates robust surface rejection capability of the *iZIP*.

### 3.3. *iZIP Interleaved Design*

---

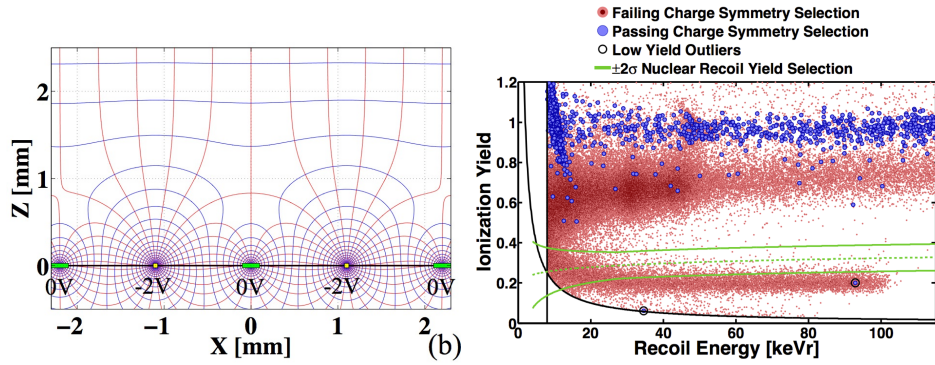


Figure 3.5: (Left) The electric field and potential lines produced from the phonon rails (yellow) and charge electrodes (green). Notice that the unique surface E-field extends  $\sim 1$ mm into the crystal and therefore surface events within this margin should exhibit asymmetric charge collection. (Right) Data from T3Z1 showing surface event discrimination (discussion in main text). Internal CDMS figure, used with permission, from [34].

# Chapter 4

## Data Acquisition

This chapter rapidly specializes, relative to the discussion of previous chapters, on the topic of Data Acquisition (DAQ) for SuperCDMS SNOLAB. We limit this chapter further by omitting in-depth discussion of the readout electronics and focus on the overall framework and various software elements of the proposed DAQ architecture.

Each iZIP will have a Detector Control and Readout Card (DCRC) connected to the upstream amplifiers and filters of the 12 phonon and 4 charge channels, and it will be continuously digitizing these signals. One substantial upgrade from previous generations of the CDMS electronics is now the existence of deadtime-less triggering and read out. Instead of halting digitization upon read out, the DCRC can simultaneously read out waveforms from triggers and digitize the incoming data stream (further discussion below).

This parallelization of processes is powerful in other ways as well. For example, our DAQ system plans to take advantage of the DCRC's ability to read out very long traces ( $\sim 50\text{ms}$ ) without a livetime penalty. At the SuperCDMS Soudan experiment, excess low frequency noise dominated other sources of TES noise and severely degraded the iZIP energy resolution. As shown in figure 4.1, the long-trace readout probes low frequencies which will allow us to filter this noise if it exists. Optimally filtering these waveforms is discussed in much further detail in chapter 5.

The DAQ system also plays an important role in the high statistics calibration runs. These runs, accomplished with different radioactive sources, are critical to understanding the energy signature of background particles and to ensure that a background event will never be mistaken for a WIMP. We discuss this, and other, fundamental features of the DAQ system below.

### 4.1 The DCRCs

The DCRC is the fundamental piece of DAQ hardware and these single compact boards have replaced the Front End Boards (FEBs), Readout Trigger Filter (RTF) boards, and bulky digitizers from previous generations of

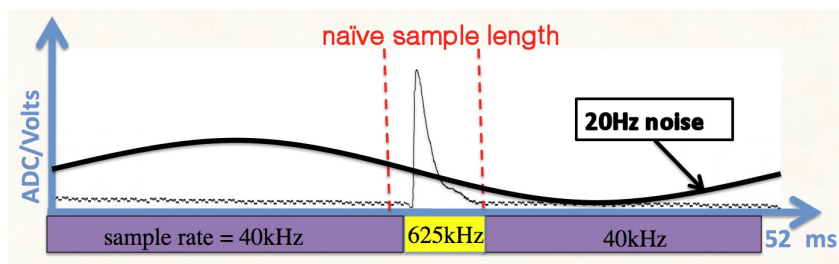


Figure 4.1: Cartoon showing the proposed phonon waveform readout and the ability to monitor low frequency noise. Hybrid waveform readout is discussed in chapter 5.

CDMS. The DCRCs continuously digitize the analog signal from the 12 phonon and 4 charge channels at 2.5Mhz (charge) and 625kHz (phonon) and write each channel to a circular memory buffer. This memory buffer is large enough to store several seconds worth of data bins.<sup>2</sup> The digitizer on the DCRC does a 14-bit analog to digital conversion.



Figure 4.2: A Rev C DCRC. The 50-pin connector interfaces with the bias and sensor lines to the detector. The board receives power over the ethernet and also communicates with the DAQ through the ethernet port.

The DCRC is also responsible for determining where triggers occur within the circular buffer and recording the time stamps. Trigger decisions are then made on the data in the circular buffer and triggers are read out before the data are overwritten (discussed further in section 4.2).

A Field Programmable Gate Array (FPGA) on the DCRC allows for a significantly fancier SuperCDMS SNOLAB trigger algorithm than was pos-

<sup>2</sup>The Rev C version DCRC has a 3.3 second buffer, but the buffer capacity will be larger on later versions.

sible with the previous electronics. The standard trigger algorithm is to look for the rising edge of pulses by setting a threshold and triggering on excursions of the ADC value above the baseline that exceed the threshold. In experiments seeking to lower thresholds and increase sensitivity to low energy events, there are clear disadvantages to this simple algorithm. The DAQ system will improve the trigger by integrating into the algorithm information about the noise characteristics and the expected pulse shape. The computational speed permitted by the FPGA allows for a finite impulse response (FIR) filter to be continuously applied to some finite length of bins in the circular buffer from which a pulse amplitude can be estimated. The FIR coefficients will be computed based on the noise pulse spectral density (PSD) and pulse shape.

Optimal coefficients for the FIR are given by the optimal filter time domain weights. While optimal filters are generally thought of in the frequency domain, they can also be computed more efficiently ( $O(N)$  vs.  $O(N \log N)$ ) in the time domain after first inverting a matrix. As will be discussed in much more depth, equation 5.14 is an example of such a time domain calculation.

## 4.2 MIDAS and the Software Front Ends

Immediately downstream of the DCRCs are the software front ends which are written using the MIDAS (Maximum Integrated Data Acquisition System) package. The front end code is in C++, but the open source MIDAS package comes with a vast array of desirable DAQ features already build in [35].

The MIDAS front ends interact with the circular buffer and trigger stamp buffer on the DCRCs and decide which of these data get written to disk. The cartoon figure 4.3 displays this interaction of the front ends with one DCRC, but what it leaves out is that the front ends will be making decisions based on and interacting with data from an entire tower (i.e. 6 DCRCs).

In the first step, delineated by (1) in the figure, the trigger front end program reads in the time stamps from the trigger buffer. It decides which triggers to read out based on the time stamps and from which iZIP the trigger occurs. The most basic of these decisions will reject triggers that occur within some short (and adjustable) time of each other. These piled-up events spoil each other because event energy, position, and timing algorithms in the downstream analysis depend heavily on pulse shape. Figure 4.4 (left) shows two piled-up events.

### 4.3. The DCRC Driver

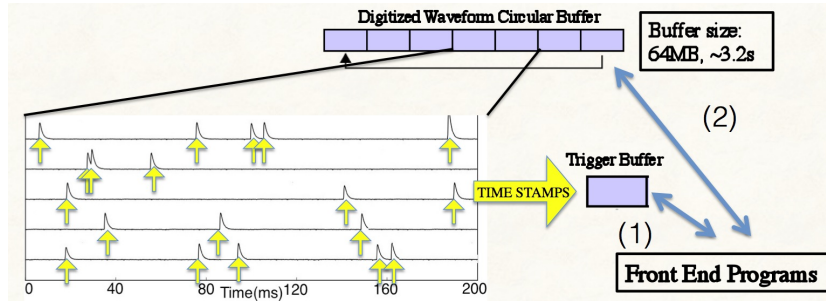


Figure 4.3: A cartoon roughly depicting the communication between the trigger front end, tower front end, the DCRC’s trigger buffer, and the DCRC’s circular buffer. The hypothetical data stream shows triggers labeled with yellow arrows. The time stamps of the triggers are continuously recorded in the trigger buffer and periodically read out by the trigger front end. The triggers with yellow arrows too close together would be rejected as piled-up while the other triggers would be read by the tower front end from the circular buffer.

The trigger front end programs then transfer the list of time stamps of triggers that have passed the decision algorithms to a second front end, called the tower front end. In the second step, delineated by (2), the tower front end accesses the DCRC circular buffer and reads out a predetermined (and adjustable) number of bins around all of the triggers. These waveforms are then written to disk.

The trigger front end and tower front end communicate with each other in a loop, and communicate with the DCRC when new triggers have been recorded, such that good triggers are never lost. In one iteration of this loop, the process of reading from the circular buffer takes significantly longer than the other steps combined.

## 4.3 The DCRC Driver

The most interesting and powerful aspects of the DCRC and MIDAS relate to detector readout discussed above, but the DCRC and MIDAS are also responsible for detector settings control. The settings fit into 6 general categories: Phonon, Charge, LED, Test Signal, Trigger, and General. Each category holds individual settings; for example, in the Charge category, the user can set the voltage bias to be applied across the detector, and set DC voltage offset of the signal arriving from the charge amplifier. The “DCRC

### 4.3. The DCRC Driver

---

driver” is the fundamental program that handles the settings control. A section of the DCRC’s hard memory is reserved for these settings, which are organized into registers. Some settings that require a large dynamic range (i.e. many bits) take up multiple registers. Conversely, because some settings are booleans or a small number of bits, some registers hold many more than 1 setting. The MIDAS “Online Database” (ODB) offers a convenient layout of settings for automatic or manual setting adjustment. The ODB is also the primary means of communication between the user and the DCRC, which is done through the DCRC driver.

The DCRC driver program is written as a MIDAS process. It should be running whenever the trigger front end and tower front end (described in section 4.2) are running. The DCRC driver constantly monitors the variables in the 6 categories in the ODB, checking for any change to occur in any of the settings.

The consistent monitoring of variables is done via the MIDAS “hotlink” functionality, which links any change in a specific ODB variable to a specific function call [35]. I have written the linked functions, which to first order :

- check that the setting has been changed to an allowed value
  - some settings have an allowable range (the detector bias range is  $-2V \rightarrow +2V$ ), while others have discrete allowed values (the driver gain must be 1,2,4, or 8)
- identify and recompute the register corresponding to the setting that has been changed
- through a TCP/IP connection to the DCRC, write the new register value to the DCRC
- if the register is successfully written to, update a special section of ODB (which we label the “Readback” section), which contains all the current DCRC settings
  - note that this step is necessary because, due to our design choices, the normal section of the ODB in which the user changes settings does not necessarily reflect the current settings on the DCRC
  - i.e. if a setting is changed to a disallowed value and therefore rejected or the writing to the DCRC fails, this will not affect the normal section of the ODB

Through these steps the DCRC driver successfully propagates any changes in the ODB to the DCRC registers. The DCRC itself then subsequently changes the settings on the detector or to components on the DCRC board.

## 4.4 Detector Testing Tools

The MIDAS “analyzer” class puts in place a convenient means of real-time viewing of waveforms as MIDAS takes them from the tower front end local memory and writes them to disk. Internal to MIDAS there is a separate separate data buffer, the SYSTEM buffer, through which the writing to hard disk occurs [35]. The SYSTEM buffer is stored in Random Access Memory (RAM) and therefore the analyzer class takes advantage of the fast access and reading of the data as it moves through this buffer.

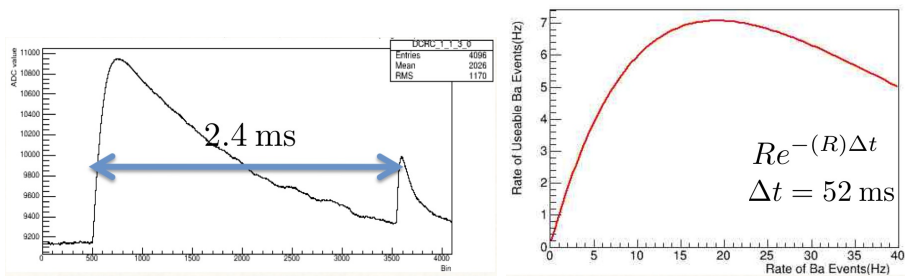


Figure 4.4: (Left) Two iZIP phonon pulses that are piled-up. (Right) The rate of usable (non piled-up) events vs. the raw event rate. For this plot a 52ms long trace has been assumed (since this is the proposed data acquisition rate trace length), where an optimal raw rate is  $\sim 20\text{Hz}$  giving a  $\sim 7\text{Hz}$  usable rate.

GUIs are being written to display the waveforms that are read out, and one of these is shown in figure 4.5. As the GUI displays replace physical oscilloscopes for displaying data, the freedom to cater the GUI design to the needs of test facilities presents significant advantages. This is especially true because SuperCDMS SNOLAB will scale up the number of iZIP/HV detectors substantially (15 to  $\sim 50$ ) and the number of phonon channels by an even larger fraction (120 to  $\sim 600$ ). Each phonon channel, whether for testing or for WIMP search, must be tuned before it becomes operable. Because manual detector tuning is relatively simple but time consuming, the MIDAS GUIs will be used to automate this laborious aspect of test facility running.

## 4.4. Detector Testing Tools

Currently GUIs are being written to accomplish these automation tasks, namely SQUID tuning, “IBIS,” and “Complex Impedance” tools. Detailed discussion of these tuning procedures are omitted, however figure 4.6 shows one of the GUIs already written for user-friendly tuning of the the phonon amplifier components.

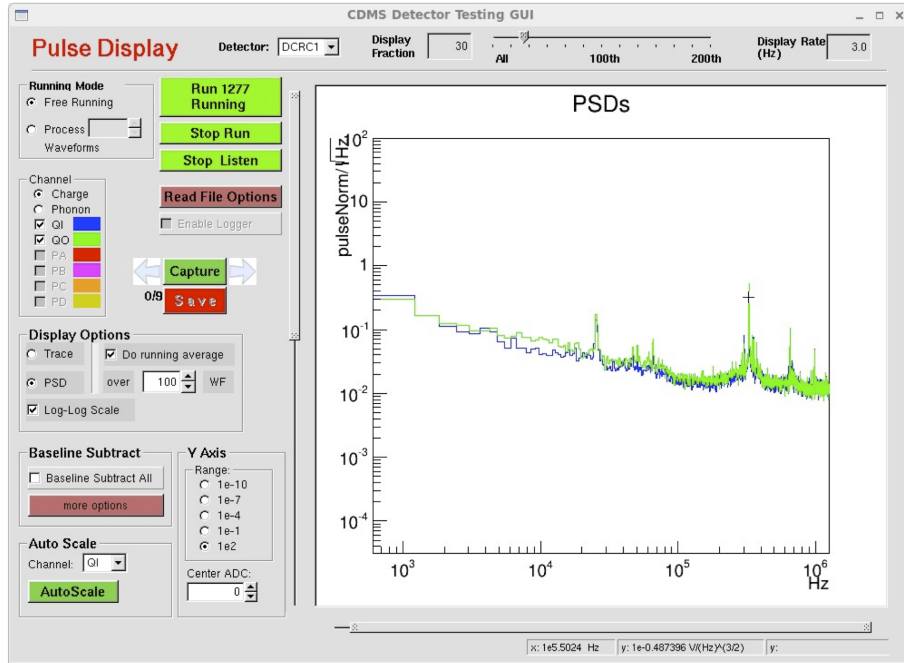


Figure 4.5: A screen shot of the Pulse Display displaying the PSD of two charge channels in real time. Behind the scenes, the time domain traces are grabbed from the SYSTEM buffer which are then Fourier transformed, and displayed on the screen.

### 4.4.1 The Pulse Display

I wrote the Pulse Display GUI (a screen shot of which is shown in figure 4.5), which displays waveforms in the time and frequency domain with oscilloscope-like user control. This is a critical and the fundamental detector testing tool for test facilities.

The GUI is build using ROOT GUI classes. All of the widgets shown in figure 4.5 are objects of the numerous ROOT GUI classes (e.g. TG-TextButton ,TGNumberEntry , TGSlider , TGTexEntry , etc.) [36]. The

object-oriented C++ framework, off of which ROOT is based, is central to the GUI's functionality. The layout of the GUI is organized in the `GuiMainFrame` class, where the frames, buttons, sliders, check boxes, etc. are given colors, sizes, positions, etc.

An instance of the `GuiMainFrame` class is created in a separate class, `PulseDisplay`, which handles the functionality of the buttons. Similar to the MIDAS "hotlink" functionality described above, function calls are linked upon the pressing of a button. A brief description of the buttons is now given, from roughly top to bottom on the GUI.

With the 'Detector' button, the user selects which DCRC to see data from. The 'Display Fraction' slider selects the fraction of events to display on the screen and the selection is indicated in the number entry to the left of the slider. The necessity of the 'Display Fraction' option is discussed below in regard to the throughput capabilities of the GUI.

From the 'Running Mode' frame, the user has the option to put a restriction on the number of waveforms to be gathered and displayed. In 'Free Running' mode (default) there is no restriction but with the 'Process  $N$  Waveforms' option selected, the number entry will become enabled, allowing the user to choose some number of waveforms to display (default=1000) before stopping the display.

The 'Start Run' frame holds some of the most important features, because the main button starts a MIDAS run and starts displaying data. Note that the frontends (`triggerfe2`, `towerfe3`) must be running for data to be displayed because the data must be moving through the SYSTEM buffer. If the frontends are not running, no traces will be displayed, but the GUI will not hang. Once the button is pressed the text turns to 'Stop Run,' and clicking it again stops displaying data and stops the MIDAS run. The 'Listen' button starts displaying data by "listening in" to an already ongoing run. It therefore requires that the frontends are running and that a run has been started. Once the button is pressed the text turns to "Stop Listen." Clicking it again stops displaying data but leaves the run going.

The 'Read File Options' frame offers some less-used features. It initiates a popup window in which the user can select the directory and file name of the MIDAS file to read. These MIDAS files contain data that has been taken in the past. The reader expects `.mid.gz` files (the typical files generated by the MIDAS logger). Clicking the 'Read' button starts reading the file. Clicking the right arrow key on the main GUI window iterates waveform-by-waveform through the file.

With the 'Channel Selection' frame the user selects the channel to display. Currently, there's no way to display charge and phonon channels si-

#### 4.4. Detector Testing Tools

---

multaneously because of the different sample rate of the charge and phonon waveforms.

Pressing the ‘Capture’ button captures the currently displayed trace or PSD and displays it on the screen. This button also enables the two arrows, allowing the user to backtrack over traces PSDs (in case the user didn’t press ‘Capture’ sufficiently quickly to see an interesting trace). There is a 10 trace/PSD buffer implemented, and the number entry “ $N/9$ ” says where the user is in the buffer. When in ‘capture mode,’ clicking the ‘Save’ button saves the displayed trace to a .root file in the home directory of the Pulse Display.

In the ‘Display Options’ frame, with the ‘Trace’ option selected (default), raw traces are displayed. With the ‘PSD’ option, the power spectral density of the trace is computed by doing a FFT on the trace, and taking the magnitude. Within either of these modes, the ‘Do Running Average’ button can be checked, where a running average of either the traces or the PSDs is computed as the data comes in, and is displayed. The buffer size of the running average can be changed at any time, without having to start from scratch in computing the average.

Clicking ‘Baseline Subtract’ activates a popup window. With both ‘Subtract Baseline’ and ‘Auto’ checked (both buttons are part of the popup window, and therefore not shown in the figure), a running average of the prepulse baseline mean is computed and the entire pulse is subtracted by this amount. The ‘Auto’ check box can be un-checked which stops the computing of the running average, but the pulse is still subtracted by whatever value exists in the running average. This functionality is important in case someone wants to use the DC offset of the ODB and see the change on the Pulse Display. The slider also allows shifting of the trace/PSD.

In the ‘Y Axis’ frame, the different buttons control the ADC Range, which is also controlled by the slider which is parallel to the Y axis. The ‘Center ADC’ displays and controls the ADC value of the center of the Y Axis, which is also controlled by the slider parallel to the Y axis.

Last, in the ‘Auto Scale’ frame, selecting a channel to autoscale and pressing the ‘AutoScale’ button scales the Y-axis to the selected channel.

Behind the scenes of the Pulse Display, it is critical to interface with the MIDAS “analyzer” class efficiently in order for the Pulse Display to operate like an oscilloscope. If significant lag exists between when traces are digitized and when traces are displayed on the screen the user will be looking at old data. Of course, this lag will typically grow in time, and it is therefore important to identify bottlenecks in the data stream. First, when grabbing traces from the SYSTEM buffer, the code uses the “GET RECENT” option

## 4.5. Readout Modes

so that the most recent data from the buffer is obtained [35]. Second, even the smallest memory leaks must be eliminated because, with continuous allocation and deallocation of memory for the traces, any memory leak will continue to grow until the machine is ground to a halt. Third, a bottleneck exists between the the ROOT GUI classes and the display to the monitor. Because display of traces at any rate greater than 60Hz is not generally differentiable from 60Hz to the human eye, the ‘Display Fraction’ option allows the user to adjust the fraction of displayed events, widening the bottleneck, and ensuring that no lag occurs.

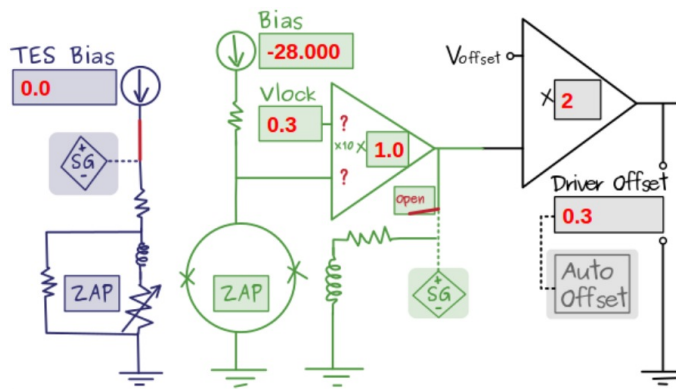


Figure 4.6: A screen shot of one of the existing detector control GUIs, written primarily by A. Roberts. The detector settings (the values in red) are controlled by the user. Internal CDMS figure, used with permission.

## 4.5 Readout Modes

Calibration runs involve higher event rates than WIMP search runs and therefore we design a DAQ system to handle this throughput. If we readout calibration data in the same manner as WIMP search data, the throughput would be unmanageable. Here we describe our intelligent DAQ system that collects the calibration data quickly, without compromising DM search time and avoiding unmanageable data throughputs.

In this effort we use different readout methods for the different calibration runs and WIMP search runs. In WIMP search mode (low background), because the event rate is so low, we plan to read out every detector when any trigger is issued from any detector. In addition, the pileup rejection within the trigger front end will be turned off.

#### 4.5. Readout Modes

---

When exposing the detectors to a gamma (Barium) or neutron (Californium) source, the DAQ is put into a “selective” readout mode where, for a given trigger, the only detector that is readout is the one that has issued the trigger. Figure 4.4 (right) demonstrates part of the importance of “selective readout.” The plotted function is  $f(R) = Re^{-R(52\text{ms})}$ , which is the rate of non-piled up events in the detector given a raw rate of  $R$  events. This is derived by noting that the probability that a random event (a poisson process) will occur at least  $\Delta T$  52ms after a previous event is given by  $e^{-R(52\text{ms})}$ . Therefore, if we are to calibrate our detectors with an optimal rate, we should create a raw rate of 20Hz, giving a usable rate of 7Hz. With this relatively high rate (reading out  $\sim 1/3$  of the total data stream coming from each detector) it is clearly important that “selective readout” be implemented, and only the detector issuing the trigger be readout.

## Chapter 5

# The Hybrid Optimal Filter

At SNOLAB it is proposed that we read out phonon and charge traces using two different sampling rates. We refer to this as ‘hybrid sampling,’ and fig. 5.1 shows the proposed sampling scheme. The slower sampled regions are generated by averaging every 16 samples of the raw digitized waveform in those regions (the data is hexadecimated). We do this because we require high resolution pulse information, long traces (for measuring low frequency noise), and reasonable data throughput; hybrid sampled traces allow us to meet these otherwise conflicting requirements. The charge/phonon pulse is captured largely within the fast sampled region, which probes the smaller time scales of the pulse, while the long time length of the traces probes frequencies down to  $\sim 19\text{Hz}$ . Thus, the total data volume is suppressed by a factor of  $\sim 16$  without losing important information.

In this chapter we show how to do a computationally efficient hybrid optimal filter (HOF), and demonstrate its good performance relative to 1D OFs that require more data. Additionally, we will use Jeff Filippini’s notation from Appendix A of his thesis where  $A$  is the template,  $S$  is the signal, and  $J$  is the noise PSD [37].

The central complication of optimal filtering hybrid waveforms is that the frequency domain no longer exhibits the convenient properties assumed for a 1D optimal filter. Namely, gaussian random noise that is non-uniformly sampled in the time domain does not have independent frequency components. Power aliasing is the primary effect at work in ruining the orthogonality between the Fourier modes—the process of averaging the fast-sampled time domain data aliases higher frequency components into the slow-sampled data, as described in sec. 5.2. This introduces correlations between different frequencies, which are represented by off-diagonal elements in the covariance matrix. We include these frequency correlations in the HOF pulse amplitude fit, where the variance of the noise components, the PSD  $J$  in eq. 5.1,

$$\chi^2(a) = \sum_n^N \frac{|\tilde{S}_n - a\tilde{A}_n|^2}{J_n} \quad (5.1)$$

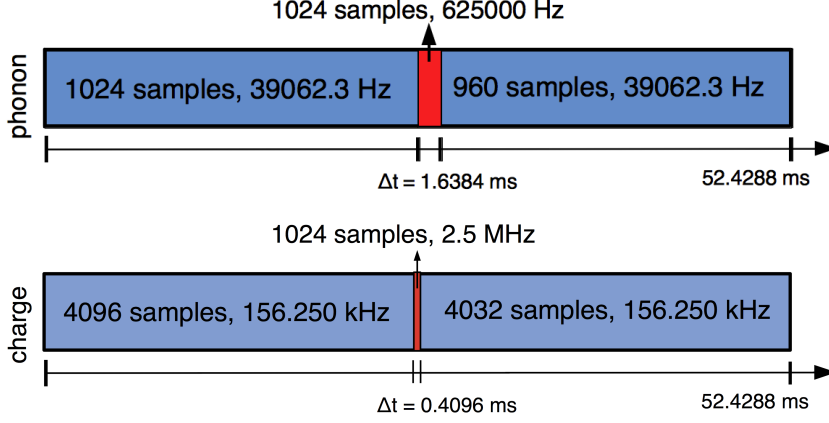


Figure 5.1: Sampling scheme for phonon and charge traces. Roughly to scale.

is replaced by the full covariance matrix  $\tilde{\mathbf{V}}$ :

$$\chi^2(a) = \sum_{i,j}^N (\tilde{S}_i - a\tilde{A}_i)(\tilde{\mathbf{V}}^{-1})_{ij}(\tilde{S}_j - a\tilde{A}_j). \quad (5.2)$$

In this notation, the  $n$ ,  $i$ , and  $j$  subscripts represent the Fourier indices, and  $\tilde{A}$  and  $\tilde{S}$  are the Fourier transforms of the template and signal, respectively. The amplitude of the signal, the value being fitted for, is given by  $a$ .

Section 5.1 presents an interpretation of the frequency domain of the hybrid waveforms. We note, however, that the non-diagonality of noise in the frequency domain makes it no more preferable than the time domain when evaluating eq. 5.2. Removing the tildes and using the time domain  $\mathbf{V}$  is equivalent and is slightly more efficient (discussed in sec. 5.5). We still include sec. 5.1 to build some intuition for the HOF in terms of 1D optimal filters, to mention some unsuccessful attempts to use non-uniformly sampled Fourier techniques to solve this problem in the framework of 1D optimal filters, and to clarify points such as the appropriate summation bounds of eq. 5.2.

We devote sec. 5.4 to discussion of the covariance matrix,  $\mathbf{V}$ . In particular we address issues that arise from its large dimension, which is equal to the number of samples in the hybrid trace (phonon: 3008; charge: 9152). We describe the most numerically stable and efficient method of determining and inverting matrices of this size and type (symmetric, positive definite).

### 5.1. Fourier Transform of a Hybrid Trace

Phonon	$R$ (Hz)	$N$	$T$ (ms)	$\Delta f$ (Hz)	$\Delta t$ (ms)	$f_{Nyq}$ (Hz)
fast	625000	1024	1.6384	610.3515	0.0016	312500
slow	39062.5	2048	52.4288	19.0735	0.0256	19531.25

Table 5.1: Important time and frequency values for hybrid phonon waveforms.

Most notably, we found that instead of building  $\mathbf{V}$  from many hybrid sampled random trigger noise traces,  $\mathbf{V}$  should be determined from noise traces that are un-averaged and read out uniformly at the fast sample rate. Doing so will save live-time and will also reduce the overall data size required to reliably determine and invert  $\mathbf{V}$ .

In my results in sec. 5.6, I show that going through the process of determining and inverting the covariance matrix pays off in the pulse amplitude resolution. We also show that the time offset estimation does not suffer from this readout scheme. We compare pulse amplitude estimation performance of this hybrid optimal filter with other 1D optimal filters under different monte carlo generated noise conditions (e.g. white,  $1/f$  + white,  $\delta$  + white). We show that the HOF performs just as well as a regular OF that uses the 52.4288 ms non-averaged waveforms, and the HOF therefore serves its purpose of filtering low-frequency noise while reducing our data size by a factor of  $\sim 16$ .

## 5.1 Fourier Transform of a Hybrid Trace

Throughout this section we will primarily discuss phonon traces, noting that the hybrid charge traces can be treated analogously.

First, it is useful to identify the important time and frequency values that are characteristic of the hybrid trace. To determine these characteristic values, it is helpful to consider the hybrid trace as two separate uniformly sampled traces. The fast sampled trace consists of just the central high frequency data; the slow sampled trace consists of all the bins of the hybrid trace with the high frequency points averaged by a factor of 16.

Tables 5.1 and 5.2 note the sample rate ( $R$ ), number of samples ( $N$ ), time span ( $T$ ), frequency resolution ( $\Delta f$ ), time resolution ( $\Delta t$ ), and Nyquist frequency ( $f_{Nyq}$ ).

Fig. 5.2 roughly displays the frequency domain spacing and range probed by the fast and slow sampled trace for the phonon waveform case, although there is a frequency range ( $610 \text{ Hz} < f < 19531.25 \text{ Hz}$ ) of overlap in which

## 5.2. Power Aliasing

Charge	$R$ (Hz)	$N$	$T$ (ms)	$\Delta f$ (Hz)	$\Delta t$ (ms)	$f_{Nyq}$ (Hz)
fast	2500000	1024	0.4096	2441.41	0.0004	1250000
slow	156250	8192	52.4288	19.0735	0.0064	78125

Table 5.2: Important time and frequency values for hybrid charge waveforms.

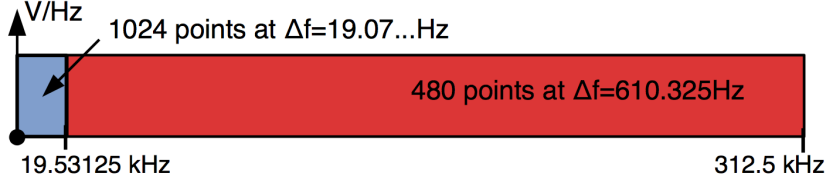


Figure 5.2: Fourier coefficient spacing for phonon waveforms.

both data sets are sensitive.

## 5.2 Power Aliasing

We initially tried to determine the Fourier coefficients by ‘pasting’ the FFT of the fast sampled data onto the FFT of the slow sampled data. As can be seen in table 5.2, the slow sampled data provides most of the low frequency information down to  $\sim 19$  Hz and up to 19531.25 Hz, in steps of  $\sim 19$  Hz. The fast sampled data provides all of the high frequency information up to 312500 Hz. For the lower frequencies in the region of overlap,  $f < 19531.25$  Hz, we only used the slow sampled FFT values because of the superior resolution of this data.

This method failed because of the problem of spectral power aliasing in the Fourier coefficients of the slower sampled data. Briefly, by sampling a signal at a uniform frequency  $f$ , you lose information about any frequency components of the signal exceeding  $f/2 = f_{Nyq}$ , the Nyquist frequency. The spectral power from frequencies exceeding  $f_{Nyq}$  instead are aliased into the frequency range  $(0, f_{Nyq})$ . This of course spoils the spectrum information below  $f_{Nyq}$ , and it is therefore critical to sample any signal at twice the frequency of the highest noise frequency component. Our fast sampling rate (phonon: 625kHz; charge: 2.5MHz) meets this requirement after the data goes through an upstream low-pass filter (an analog ‘anti-aliasing’ filter preceding the analog-to-digital conversion). The source of the aliasing is the low Nyquist frequency of the slow sampled data (phonon:  $f_{Nyq,slow} =$

### 5.3. Fourier Transform without the FFT

19531.25 Hz ; charge:  $f_{Nyq,slow} = 78125$  Hz), where the averaging process aliases power between  $(f_{Nyq,slow}, f_{Nyq,fast})$  into the range  $(0, f_{Nyq,slow})$ .

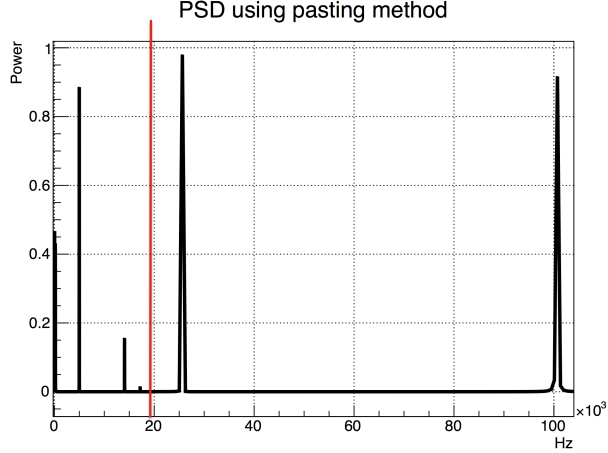


Figure 5.3: A PSD, using the the pasting method, of a hybrid phonon trace with certain injected frequencies. There are aliased peaks at  $f=14.062$ kHz and  $f = 17.186$ kHz (discussed in main text). The red line marks the folding point,  $f_{Nyq,slow}$  at 19531Hz.

The frequency spectrum in fig. 5.3 demonstrates the aliasing, and was generated using the pasting method of a hybrid phonon trace that consisted of five sinusoidal signals. The signals had frequencies 50Hz, 200Hz, 5kHz, 25kHz, 100kHz, all of amplitude 1. The peak at  $\sim 14$ kHz is clearly due to aliasing and can be attributed to the true signal at 25kHz mirrored around  $f_{Nyq,slow}$ :  $19.531 - (25 - 19.531) = 14.062$ . The smaller feature at  $\sim 17$ kHz is also due to aliasing and can be traced back to the true 100kHz signal:  $19.531 - (100 - 5 \times 19.531) = 17.186$ . The smaller amplitude of this feature should not be surprising because we expect at least some of the power at the higher frequencies is ‘washed out’ by the averaging process. The derivation of where aliased frequencies occur is in Appendix B.

### 5.3 Fourier Transform without the FFT

There are many algorithms in existence for calculating non-uniform discrete Fourier transforms (NDFTs) for the many applications where you have data spaced randomly, or somewhat randomly, in the time domain. One can even compute a robust NUFFT—a non-uniform fast Fourier transform—in

### 5.3. Fourier Transform without the FFT

---

$O(N \log(N))$ , by diffusing your data onto an evenly spaced time domain grid, applying the FFT, and then dividing out the FFT of the diffusion. References [39] (the original paper) and [40] (*Accelerating the Nonuniform Fast Fourier Transform*) have solved this problem in two and three dimensions. The Lomb-Scargle periodogram [42] is another technique with which we experimented. However, neither of these NDFTs are designed to exploit the high degree of symmetry in our time domain data, and we therefore do not use them.

I do exploit these symmetries (i.e. only two different time domain spacings) with my own  $O(N)$  non-uniform discrete Fourier transform. However, most importantly, regardless of the performance of my or other NDFT techniques, because the frequency domain is not one in which the noise is diagonal, any frequency domain optimal filter fit that neglects correlations between frequency components will be suboptimal. Therefore, the content of this and the rest of section 3 is not explicitly used in my solution to the general problem, which is developed in sec. 5.5.

The discrete Fourier transform (DFT) of a time series  $g_k$  is given by:

$$\tilde{g}_n = \frac{1}{N} \sum_{k=-\frac{N}{2}}^{\frac{N}{2}-1} g_k e^{-2\pi i f_n t_k} \quad (5.3)$$

where  $\tilde{g}_n$  is evaluated for  $n = -\frac{N}{2} \rightarrow \frac{N}{2} - 1$  in integer steps. The inverse DFT (IDFT) is

$$g_k = \sum_{n=-\frac{N}{2}}^{\frac{N}{2}-1} \tilde{g}_n e^{+2\pi i f_n t_k}. \quad (5.4)$$

For a real-valued  $g_k$  there is a symmetry in the Fourier coefficients about the zero frequency:

$$\tilde{g}_n = \tilde{g}_{-n}^*, \quad (5.5)$$

which ensures that the number of independent points in the time and frequency domain are equal.

For uniformly sampled data at a rate  $R$  spanning a time  $T$ ,  $f_n = \frac{n}{T}$ , and  $t_k = \frac{k}{R}$ . With  $R \times T = N$  data points, the argument of the exponent becomes  $\frac{-2\pi i n k}{N}$ .

The values of  $f_n$  and  $t_k$  are not as simple for the hybrid trace, as will be seen in the following two sections. Due to this added complexity, it is impossible to explicitly write the hybrid DFT/IDFT as cleanly as eq. 5.3

### 5.3. Fourier Transform without the FFT

and 5.4. We instead use a matrix  $\mathbf{A}$  to accomplish the IDFT:  $\vec{g} = \mathbf{A}\tilde{\vec{g}}$  and its inverse to accomplish the DFT:  $\tilde{\vec{g}} = \mathbf{A}^{-1}\vec{g}$ .

Determining  $f_n$  and  $t_k$  for the hybrid traces allows us to determine the elements of  $\mathbf{A}$ .

#### 5.3.1 Fourier Frequencies of a Hybrid Trace

In this section we elaborate on the Fourier frequency spacing that is roughly displayed in fig. 5.2.

It again helps to consider the Fourier frequencies of the two separate data regions: the fast sampled data and the derived slow sampled data. For the slow sampled data these are: (simply  $f_{slow,n} = n \times 19.07349\dots\text{Hz}$ )

$n_{slow}$	0	1	2	3	...	1021	1022	1024
$f_{slow,n}(\text{Hz})$	0	19.1	38.1	57.2	...	19474.0	19493.1	19531.25

The Fourier frequencies of the fast sampled data are: (simply  $f_{fast,n} = n \times 610.3515625\text{Hz}$ )

$n_{fast}$	0	1	2	...	31	32	...	512
$f_{fast,n}(\text{Hz})$	0	610.4	1831.1	...	18920.9	19531.25	...	312500.0

The hybrid trace Fourier frequencies  $f_n$  should take the  $n_{slow}$  frequencies values below the slow sampled Nyquist frequency. The slow sampled data loses sensitivity above  $n_{slow} = 1024$ , and therefore for  $f_{1025}$ , we should use  $n_{fast} = 33$  at  $f = 20141.6\text{Hz}$ , and we continue at the fast sampling Fourier frequencies up to  $n_{fast} = 512$ ,  $f = 312500\text{Hz}$ . The hybrid trace  $f_n$  are written out below:

$n$	0	1	...	1023	1024		1025	...	1504
$f_n(\text{Hz})$	0	19.1	...	19512.17	19531.25		20141.6	...	312500.0
$\Delta f_n(\text{Hz})$	-	19.1	...	19.1	19.1		610.4	...	610.4

Negative frequency coefficients are overdetermined from the symmetry of eq. A.1, and therefore not computed. Counting real and imaginary components at each Fourier frequency, it appears that we transform  $N_{\text{time}} = 3008$  time domain points to  $N_{\text{Fourier}} = 1505 \times 2 = 3010$  frequency domain points. This issue is resolved by noticing that the imaginary Fourier coefficient of the zero frequency,  $f_0$ , and of the Nyquist frequency,  $f_{1504}$ , must be zero. This proof is given in appendix A.

### 5.3.2 Time Points of a Hybrid Trace

It is also important to identify the  $t_k$  at which to evaluate the hybrid trace Fourier transform. One option is to use the  $t_k$  at the 3008 time points at which the hybrid waveform is given:

$$t_k = \begin{cases} k(0.0256) \text{ ms} & 0 < k \leq 1024 \\ (k - 1024)(0.0016) + (1024)(0.0256) \text{ ms} & 1024 < k \leq 2048 \\ (k - 2048)(0.0256) + (1024)(0.0016) + (1024)(0.0256) & 2048 < k \leq 3008 \end{cases} \quad (5.6)$$

However, this choice is suboptimal because the slow sampled portion of the waveform is obtained by averaging 16 time points, not by keeping 1 time point.

For  $0 < k \leq 1024$  and  $2048 < k \leq 3008$ , the average of the sine or cosine function over 16 time points should be used. For example, the inverse Fourier transform in eq. 5.4 becomes

$$g_k = \begin{cases} \sum_{n=-\frac{N}{2}}^{\frac{N}{2}-1} \tilde{g}_n \frac{1}{16} \sum_{j=0}^{15} \exp [2\pi i f_n (t_k + j\delta)] & 0 < k \leq 1024 \\ \sum_{n=-\frac{N}{2}}^{\frac{N}{2}-1} \tilde{g}_n \exp [2\pi i f_n t_k] & 1024 < k \leq 2048 \\ \sum_{n=-\frac{N}{2}}^{\frac{N}{2}-1} \tilde{g}_n \frac{1}{16} \sum_{j=0}^{15} \exp [2\pi i f_n (t_k + j\delta)] & 2048 < k \leq 3008 \end{cases} \quad (5.7)$$

where the  $t_k$  values are given by eq. 5.6,  $\delta = 0.0016\text{ms}$  is one of the fast time steps, and the  $f_n$  are at the spacing discussed in sec. 5.3.1.

### 5.3.3 The Transformation Matrix: $\mathbf{A}$

In the interest of using an entirely real transformation matrix, we transform real and imaginary Fourier coefficients independently. Additionally, recall that we need not compute the  $\tilde{g}_n$  for negative frequencies (since they are overdetermined by eq. A.1). Last, recall that the imaginary component of the zero and Nyquist frequency must be zero (proof in Ap. A).

Therefore,  $\mathbf{A}^{-1}$  transforms the 3008 time domain points into 3008 cosine and sine coefficients. We use  $\tilde{S}_i$  to describe these coefficients in the 3008 dimension non-orthogonal frequency domain. We write out how we have organized our  $\tilde{S}_i$  vector below in terms of the  $\tilde{g}_n$  that you would associate

#### 5.4. Determining and Inverting the Covariance Matrix

---

with the standard Fourier transform, but using the unconventional frequency spacing and time averaging.

$$\frac{\vec{S}}{\tilde{g}_n} \left| \begin{array}{ccccccccc} \tilde{S}_0 & \tilde{S}_1 & \tilde{S}_4 & \tilde{S}_5 & \dots & \tilde{S}_{3006} & \tilde{S}_{3007} \\ \text{Re}[\tilde{g}_0] & \text{Re}[\tilde{g}_{1504}] & \text{Re}[\tilde{g}_2] & \text{Im}[\tilde{g}_2] & \dots & \text{Re}[\tilde{g}_{1503}] & \text{Im}[\tilde{g}_{1503}] \end{array} \right.$$

Notice that for convenience we place  $\text{Re}[\tilde{g}_{1504}]$ , the real part of the Nyquist coefficient, as the second element of  $\vec{S}$ .

We show the third and fourth columns of  $\mathbf{A}$  below.

$$\left[ \begin{array}{c} \frac{1}{16} \sum_{n=0}^{15} \cos(\omega_1(t_0 + n\delta)) \\ \frac{1}{16} \sum_{n=0}^{15} \cos(\omega_1(t_1 + n\delta)) \\ \vdots \\ \frac{1}{16} \sum_{n=0}^{15} \cos(\omega_1(t_{1023} + n\delta)) \\ \cos(\omega_1 t_{1024}) \\ \vdots \\ \cos(\omega_1 t_{2047}) \\ \frac{1}{16} \sum_{n=0}^{15} \cos(\omega_1(t_{2048} + n\delta)) \\ \vdots \\ \frac{1}{16} \sum_{n=0}^{15} \cos(\omega_1(t_{3007} + n\delta)) \end{array} \right] \left[ \begin{array}{c} \frac{1}{16} \sum_{n=0}^{15} \sin(\omega_1(t_0 + n\delta)) \\ \frac{1}{16} \sum_{n=0}^{15} \sin(\omega_1(t_1 + n\delta)) \\ \vdots \\ \frac{1}{16} \sum_{n=0}^{15} \sin(\omega_1(t_{1023} + n\delta)) \\ \sin(\omega_1 t_{1024}) \\ \vdots \\ \sin(\omega_1 t_{2047}) \\ \frac{1}{16} \sum_{n=0}^{15} \sin(\omega_1(t_{2048} + n\delta)) \\ \vdots \\ \frac{1}{16} \sum_{n=0}^{15} \sin(\omega_1(t_{3007} + n\delta)) \end{array} \right]$$

Clearly the lower and upper bounds of  $i$  and  $j$  must be 0 and 3007, respectively, in the general pulse amplitude  $\chi^2$  in eq. 5.2.

### 5.4 Determining and Inverting the Covariance Matrix

The covariance matrix in the HOF plays the role of the PSD  $J$  in the 1D OF, and just as  $J$  is computed from many noise traces ( $J_i = \langle \tilde{g}_i^2 \rangle$ ), the frequency domain covariance matrix  $\tilde{\mathbf{V}}$  is given by the average of the outer product of noise traces:

$$\tilde{V}_{ij} = \text{E}[(\tilde{g}_i - \langle \tilde{g}_i \rangle)(\tilde{g}_j - \langle \tilde{g}_j \rangle)] = \frac{1}{M} \sum_{m=1}^M \sum_{i,j} \tilde{g}_{m,i} \tilde{g}_{m,j} \quad (5.8)$$

for  $M$  noise traces, where the  $\tilde{g}_i$  coefficients have been determined according to sec. 5.3. Here it is also assumed that  $\langle \tilde{g}_i \rangle = 0$ . The time domain covariance matrix is equivalently computed by using the time domain  $g_i$  data.

#### 5.4. Determining and Inverting the Covariance Matrix

---

	Hybrid OFs			1D OF	
				sec. 5.4.2 $\mathbf{V}$	32768 points
$M/d$	3	7	10	-	-
$\sigma_{\hat{a}}$	6.4	5.8	5.6	5.7	5.5

Table 5.3: The baseline resolution of the HOF improves as  $M/d$  increases up to  $\sim 7$ . We simulated  $1/f$  + white noise and 1000 phonon pulses (discussed further in sec. 5.6.1). The HOF approaches the limit of its best possible resolution, which is the resolution of the 1D uniform OF applied to the full 625kHz, 32768 point, trace. We also show the resolution by determining the covariance matrix as described in sec. 5.4.2, which shows good performance.

Eq. 5.8 is only an estimation of  $\tilde{\mathbf{V}}$ , which we denote  $\tilde{\mathbf{V}}'$ , and increasing  $M$  brings the estimate closer to the true covariance matrix. Inconveniently, we found that the number of noise traces required to reliably determine  $\tilde{\mathbf{V}}$  is:

$$M/d \gtrsim 7, \quad (5.9)$$

where  $\dim(\tilde{\mathbf{V}})=d$ .  $M$  is surprisingly large in comparison to uniformly sampled data where there were  $d$  independent, diagonal noise components.  $\tilde{\mathbf{V}}$  is symmetric but has  $d^2/2 + d/2$  independent elements, and therefore measuring the noise requires significantly more data and effort.

The particular ratio of eq. 5.9 was determined and verified in multiple ways. First, because all covariance matrices are symmetric and positive definite (i.e. have positive eigenvalues), negative eigenvalues of  $\tilde{\mathbf{V}}'$  are a clear indicator that  $\tilde{\mathbf{V}}$  has been poorly estimated, generally due to statistical fluctuations in the noise. Increasing  $M$  makes all eigenvalues positive. Second, because the true  $\tilde{\mathbf{V}}$  will give the best possible pulse amplitude estimation resolution, increasing  $M$  up to  $M \approx d \times 7$  and observing only small amplitude estimation resolution improvement for larger  $M$  justified the condition of eq. 5.9. Table 5.3 shows this baseline resolution improvement for simulated phonon pulses (the method of obtaining these resolutions is discussed in sec. 5.6.1).

### 5.4.1 The Ratio $M/d$

A matrix's eigenvalues are indicators of its invertibility. The existence of a zero eigenvalue of course indicates a singular (non-invertible) matrix. With an input of a nearly singular matrix, eigensolvers will compute a number of very small (e.g.  $10^{-15}$ ) and a number of very large eigenvalues. The eigenvectors with very small eigenvalues make up the nullspace of the matrix, which is the space in which the matrix will never transform any vector; a matrix that has a null space is non-invertible. The rank of a matrix,  $R$ , is the dimension of the matrix,  $d$ , minus the dimension of the nullspace.

In the process of trying to invert  $\mathbf{V}'$  (the estimate of  $\mathbf{V}$ ), looking at its eigenvalues showed a clear linear relationship between  $R$  and the number of noise traces used to build the matrix,  $M$ . The rank approximately equaled the number of noise traces,  $R \approx M$ , and this correlation was strongest for values of  $M$  much less than  $d$ .

To explain this relationship, it is important to note that every data trace can be represented as a linear combination of the true eigenvectors of the true underlying covariance matrix. This is nothing particularly special about  $\mathbf{V}$ —every data trace lies in a  $d$  dimensional space and therefore any invertible  $d$  dimensional matrix will have  $d$  orthogonal eigenvalues with non-zero eigenvalues that span the  $d$  dimensional vector space. Additionally, every data trace that has been added to  $\mathbf{V}'$  can be represented as a linear combination of its eigenvectors. From this, it would be impossible to invert  $\mathbf{V}'$  using fewer than  $d+1$  traces.

As traces are added to build  $\mathbf{V}'$ , they probe more dimensions of the full space, which is reflected in the matrix's eigenvalues. The observation that  $R \approx M$  indicates that each new trace probes one additional dimension. It might therefore be surprising that we found that  $M/d \gtrsim 7$  for reliably determining  $\mathbf{V}$ , instead of  $M/d \approx 1$ . First, we observed the  $R \approx M$  relationship weaken as  $M$  approached  $d$ , and  $\mathbf{V}'$  remained singular until  $1 \lesssim M/d < 2$ . Second, once  $M$  was increased so that  $\mathbf{V}$  was invertible, the baseline resolution of the HOF improved for larger  $M/d$ . Table 5.3 displays these results, and we report the approximate condition  $M/d \gtrsim 7$  because of the only small improvement in resolution for  $M/d \approx 10$ , which approaches the limit of the best possible resolution.

These findings represent that it is more difficult to reliably probe the final dimensions of the space. Consider an analogy with 3 randomly chosen points in 3D space. Most likely these 3 points can represent, by linear combination, any point in the 3D space—this will be true provided that one of the points is not a linear combination of the other two (i.e. does not lie on the line

#### 5.4. Determining and Inverting the Covariance Matrix

---

determined by the other two points).<sup>3</sup> Therefore, while in principle only  $d+1$  data traces are required to probe  $d$  dimensions and reliably estimate  $\mathbf{V}$ , as more noise traces are acquired, it becomes more likely that the newest trace lies close to a ‘plane’ established by (i.e. can be expressed as a linear combination of) the previous noise traces. This gives some sense for why  $M/d \gtrsim 7$  is required to reliably estimate the eigenvectors/eigenvalues of  $\mathbf{V}$ , and reliably invert  $\mathbf{V}'$ .

Due to the impractical acquisition of  $\sim 21000$  phonon and  $\sim 63000$  charge noise traces over the course of a series, we instead determine  $\tilde{\mathbf{V}}$  from  $\sim 1000$  un-averaged noise traces as described next. Unaveraged noise traces will also reduce total data throughput, as shown in section 5.8.

##### 5.4.2 Robust and Efficient Computation of the Covariance Matrix

For simplicity we discuss only the phonon waveforms in this section, noting that charge waveforms can be treated analogously; the dimension of the charge problem is just larger. Note that an un-averaged phonon waveform is 32768 samples long, and therefore has 32768 independent Fourier coefficients. We will use  $\vec{\beta}$  to describe these Fourier coefficients, which are the coefficients of the (orthogonal) sines and cosines at the standard evenly spaced frequencies for uniform Fourier transforms, and we use  $\tilde{\mathbf{V}}^\beta$  to denote the covariance matrix of this data. All the convenience of this method comes from that fact that we can assume that  $\tilde{\mathbf{V}}^\beta$  is diagonal. While this is an approximation, where non-stationary noise introduces off diagonal elements,  $\tilde{\mathbf{V}}^\beta$ 's diagonality is an assumption implicitly made when applying a 1D optimal filter to uniformly sampled data.<sup>4</sup> For this note we ignore the off-diagonal elements, and we use FFT technology to compute the diagonal components.

$$\tilde{V}_{ii}^\beta = \langle \beta_i^2 \rangle. \quad (5.10)$$

Recall that we use  $\vec{S}$  to describe Fourier coefficients in the 3008 dimension

---

<sup>3</sup>This analogy can be carried through to understand why  $d+1$ , not  $d$ , traces are required to probe  $d$  dimensions. Three linearly independent points only establish a plane; a fourth linearly independent point probes the third dimension.

<sup>4</sup>Off-diagonal elements due to non-stationary noise (i.e. eq. 39 in Rito's OF theory note [44]) could certainly be included in this framework and included in  $\mathbf{V}^\beta$ . However, computing the NSOF covariance matrix could present challenges due to the non-hexadecimated read out of real events instead of noise traces. Fortunately, no sparsification of the NSOF matrix would be needed in order to invert it, because the full propagation would still be as easy as eq. 5.12.

#### 5.4. Determining and Inverting the Covariance Matrix

---

non-orthogonal frequency domain. We know that there is a linear transformation between these two domains accomplished by a  $3008 \times 32768$  matrix, which we denote  $\mathbf{G}$ . We then propagate the uncertainty from this covariance matrix,  $\tilde{\mathbf{V}}^\beta$ , to the non-diagonal 3008 dimensional covariance matrix, denoted  $\tilde{\mathbf{V}}$ , to be used in the optimal filter. The propagation is simple once we have determined the linear transformation between the two domains:

$$\tilde{S}_i = \sum_{j=1}^{32768} G_{ij} \beta_j. \quad (5.11)$$

We determine  $\mathbf{G}$  by computing its columns explicitly, one-by-one, by the following procedure:

1. produce an un-averaged time domain trace equal to one of the orthogonal modes of the  $\vec{\beta}$  vector (i.e.  $\sin(2\pi f_n)$  or  $\cos(2\pi f_n)$  where  $f_n = n \times 19.07... \text{ Hz}$ )
  - for example,  $\sin(2\pi f_2)$  gives  $\vec{\beta} = [0, 0, 0, 0, 1, 0, 0, \dots]$
  - $\cos(2\pi f_2)$  gives  $\vec{\beta} = [0, 0, 0, 0, 0, 1, 0, \dots]$
2. downsample this waveform to obtain the 3008 sample trace
3. determine the  $\vec{S}$  coefficients of this trace by multiplying the time domain trace by  $\mathbf{A}^{-1}$ , as described in sec. 5.3. This  $\vec{S}$  vector is one column of  $\mathbf{G}$
4. repeat for each sine and cosine orthogonal mode of the  $\vec{\beta}$  basis, up to the Nyquist frequency at  $n = 16384$

It is interesting to look at the rows of  $\mathbf{G}$  because they indicate which of the 32768 orthogonal sine and cosine coefficients contribute to a single non-orthogonal 3008 sine or cosine coefficient. Fig. 5.4 makes it clear that power aliasing is scrambling the hybrid Fourier coefficients.

With the 32768 columns of  $\mathbf{G}$  determined, the variances of  $\vec{\beta}$  coefficients along the diagonal of  $\mathbf{V}^\beta$  are propagated to the variances/covariances of  $\vec{S}$  coefficients,  $\tilde{\mathbf{V}}$ , according to:

$$\tilde{V}_{ij} = \sum_{k=1}^{32768} \sum_{l=1}^{32768} G_{ik} \tilde{V}_{kl}^\beta G_{jl} \quad ; \quad \tilde{\mathbf{V}} = \mathbf{G} \tilde{\mathbf{V}}^\beta \mathbf{G}^T. \quad (5.12)$$

$\mathbf{G}$  only need be computed once because the linear transformation between the two domains is of course constant.  $\tilde{\mathbf{V}}^\beta$  and  $\tilde{\mathbf{V}}$  depend on the noise, and they must be redetermined once per series.

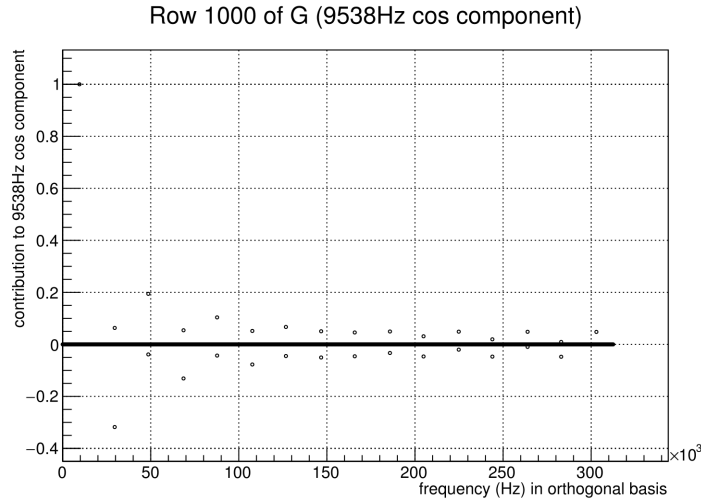


Figure 5.4: There are 16 frequency components in the orthogonal basis that contribute to the cosine coefficient at  $\sim 9538\text{Hz}$  in the non-orthogonal basis. These frequencies match the predicted alias frequencies derived in Appendix B.

### 5.4.3 Inversion by Choleski Decomposition

Choleski Decomposition is an efficient method of inverting positive definite matrices, and the decomposition gains a factor of 2 in operations count over the more standard LU decomposition. The inversion is still an  $O(N^3)$  process. Like the LU decomposition, it is a triangular decomposition but due to positive definiteness, the upper triangular matrix can be found so that it is the transpose of the lower triangular matrix. Choleski decompositions are covered thoroughly in Section 2.9 of *Numerical Recipes*[38], and they are also implemented in ROOT with the TDecompChol class.

## 5.5 Time Domain Covariance Matrix and $\chi^2$

Because the frequency domain of the hybrid waveforms is not one in which the noise is diagonal, there is no advantage to working in that domain. The frequency domain is in fact less efficient because transforming any hybrid waveform into the frequency domain requires an  $O(N^2)$  multiplication by  $\mathbf{A}$ , as discussed in sec. 5.3.

To be clear, we continue to compute  $\tilde{\mathbf{V}}^\beta$ , which uses the full uniformly

sampled noise traces, in the frequency domain. We still utilize the convenient approximation that this matrix is diagonal; but instead of propagating those variances to  $\tilde{\mathbf{V}}$ , we propagate them to the time domain covariance matrix. This follows the same procedure outlined in sec. 5.4.2, except  $\mathbf{G}$  is now a different matrix,  $\mathbf{G}'$ , which is the linear transformation from the 32768 dimension orthogonal frequency domain into the 3008 point hybrid time domain. We compute the columns of  $\mathbf{G}'$  identically as outlined in sec. 5.4.2, but we skip step 3 of the procedure. Eq. 5.12 still gives the correct propagation of variances/covariances between domains. Because we will use the hybrid time domain covariance matrix for the remainder of this note, we denote it simply by  $\mathbf{V}$ .

The tildes are then removed from the  $\chi^2$  pulse amplitude fit of eq. 5.2, which now takes the form:

$$\begin{aligned}\chi^2(a) &= \sum_{i=0}^{3007} \sum_{j=0}^{3007} (S_i - aA_i)(V^{-1})_{ij}(S_j - aA_j) \\ &= (\vec{S} - a\vec{A})^T \cdot \mathbf{V}^{-1} \cdot (\vec{S} - a\vec{A})\end{aligned}\tag{5.13}$$

and by the normal equations the best fit pulse amplitude is:

$$\hat{a} = [\vec{A}^T \mathbf{V}^{-1} \vec{A}]^{-1} \vec{A}^T \mathbf{V}^{-1} \cdot \vec{S}\tag{5.14}$$

Eq. 5.14 might seem too computationally intensive to be carried out for each trace that is read out, and it is an  $O(N)$  operation once the vector on the left side of the dot product is computed. The quantity in brackets reduces to a single number, so no matrix (other than the covariance matrix) is inverted.

## 5.6 Amplitude and Time Offset Estimation Results

In order to check the performance of the HOF, we simulate the 52.4ms pulse and noise waveforms. To build a uniformly sampled 52ms noise trace we start with an underlying noise PSD ( $J$ ). We then generate the Fourier transform of the trace by randomly drawing the cosine and sine coefficients from appropriate gaussian distributions; at frequency  $f_k$  the gaussian distribution has  $\mu=0$  and  $\sigma = \sqrt{J(f_k)}$ . Applying an IFFT gives the desired time domain noise trace. If a realistic pulse is desired, the pulse template, scaled to a certain amplitude, is added to the noise.

### 5.6.1 Phonon Pulse Simulation

We compare the pulse amplitude resolution,  $\sigma_a^2$ , of the HOF to different 1D optimal filters. With the ability to generate realistic noise and pulse waveforms that are uniformly sampled at 625kHz and 52.4288ms long, we test (1) the HOF with the 3008 point downsampled waveform, (2) a 1D OF using the 32768 point full waveform, (3) a 1D OFs using 1024 points (1.64ms), and (4) a 1D OF using 2048 points (3.28ms).

The covariance matrix for the HOF is computed using 1000 full waveform noise traces. PSDs for the 1D OFs are computed from the appropriate sections of the same 1000 noise waveforms.

For the template,  $A$ , we use the double decaying exponential functional form:

$$A(t) = A_f \left[ 1 - \exp\left(-\frac{t - T_f}{R_f}\right) \right] \exp\left(-\frac{t - T_f}{F_f}\right) + A_s \left[ 1 - \exp\left(-\frac{t - T_s}{R_s}\right) \right] \exp\left(-\frac{t - T_s}{F_s}\right) \quad (5.15)$$

to generate the discrete time domain points,  $A_k$ . Fig. 5.5 shows an example of the uniformly sampled 52.4ms template; the inset shows the template for the 1024 point OF, which is also the fast sampled portion of the hybrid waveform.

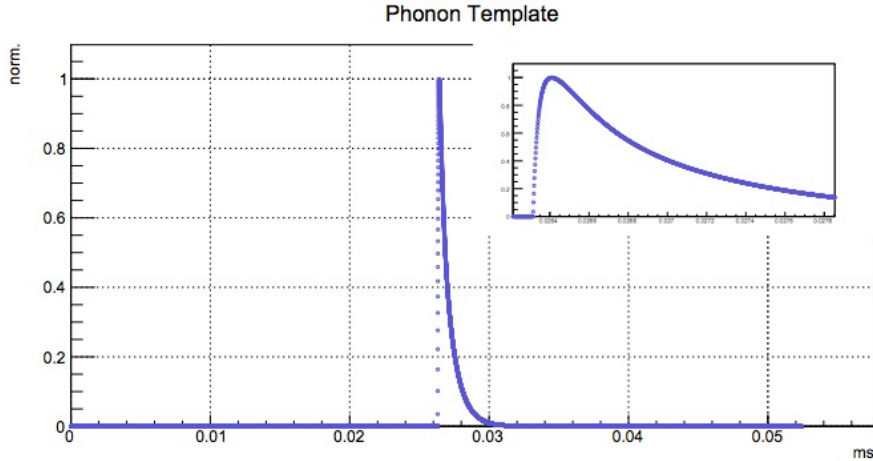


Figure 5.5: A phonon template, with  $A_f = 0.9, T_f = 2771\mu s, R_f = 25\mu s, F_f = 175\mu s, A_s = 0.4, T_s = 2771\mu s, R_s = 100\mu s, F_s = 816\mu s$ . The inset shows the 1024 points of fast sampled data.

### 5.6.2 Pulse Amplitude Resolution

For the table below, we perform the 4 different OFs on 10000 simulated signals with amplitude 100 and measure the amplitude resolution,  $\sigma_{a=100}^2$ . We also measure a baseline resolution for 10000 signals with amplitude 0, with the time offset search turned off, denoted  $\sigma_{BL}^2$ . We report only  $\sigma_{BL}^2$  because it was found to be statistically equivalent to  $\sigma_{a=100}^2$ . For the 1D optimal filters we also report the expected resolution,  $\sigma_{EX}^2$ , given by:

$$\sigma_{EX}^2 = \left[ \sum_{n=-\frac{N}{2}}^{\frac{N}{2}-1} \frac{|\tilde{A}_n|^2}{J_n} \right]^{-1} \quad (5.16)$$

For each noise model, we normalized the PSD such that expected amplitude estimate resolution of the 32768 point OF would equal 9.0, as shown in the table for  $\sigma_{EX}^2$ .

Looking down the columns of table 5.4, the resolutions decrease as expected for the longer 1D OFs, and also agree with the expected resolution. Also, the 3008 point HOF performs equally well as the full 32768 point OF.

As you go to longer traces, the expected resolution of eq. 5.16 gets better for a number of reasons. You begin to more finely resolve the changes in the template and the PSD, which allows for an optimal filter  $\frac{\tilde{A}_n^*}{J_n}$  which does a better job of weighting the frequencies with the best signal-to-noise. Equivalently, the longer traces brings the sum in eq. 5.16 closer to its continuous analog:

$$\sigma_{EX}^2 = \left[ \int df \frac{|\tilde{A}(f)|^2}{J(f)} \right]^{-1}, \quad (5.17)$$

which tracks the continuous variations of  $\frac{|\tilde{A}(f)|^2}{J(f)}$ , and by resolving the features of the integrand the area is maximized. For example, if there is no difference between the signal-to-noise at  $f = 20\text{Hz}$  vs.  $f = 100\text{Hz}$ , you pay no penalty by weighting these bins equivalently in the optimal filter—a frequency sensitivity of  $\Delta f = 80\text{Hz}$  is equally optimal as  $\Delta f = 20\text{Hz}$  (for the example of these two bins). But we expect that low frequency features in the PSD and template will not make  $\frac{|\tilde{A}(f)|^2}{J(f)}$  constant from  $f = 20\text{Hz}$  to  $f = 100\text{Hz}$ , and so  $\Delta f < 80\text{Hz}$  is optimal.

Longer traces also reduces power leakage from frequency-to-frequency, because  $\Delta f$  decreases, which also increases the sum. Additionally, and most importantly, since the template  $|\tilde{A}|$  is largest at the lowest frequencies, it is extremely beneficial to measure the lowest frequencies down to  $\sim 19\text{Hz}$ , and

5.6. Amplitude and Time Offset Estimation Results

		Noise Models					
		white (wt.)	$1/\sqrt{f}$ + wt.	$1/f$ + wt.	$1/f$ +wt.+ $\delta$	$1/f$ +wt.+ $\sim$	
1024	point OF	$\sigma_{BL}^2$	10.2	10.96	11.22	16.6	18.4
		$\sigma_{EX}^2$	9.0	9.8	11.4	14.9	17.7
2048	point OF	$\sigma_{BL}^2$	9.12	9.0	9.42	11.56	17.19
		$\sigma_{EX}^2$	9.0	9.0	9.24	11.4	17.2
32768	point OF	$\sigma_{BL}^2$	9.12	9.18	9.18	9.18	8.76
		$\sigma_{EX}^2$	9.0	9.0	9.0	9.0	9.0
3008	point HOF	$\sigma_{BL}^2$	9.01	9.18	8.91	8.9	9.0

Table 5.4: Baseline and expected resolution of different length 1D OFs and the HOF. The HOF performs as well as the 32768 point 1D OF. The uncertainty on the resolutions is  $\sigma_{\sigma^2} = \sigma^2 \sqrt{\frac{2}{N-1}}$ , so  $\sigma_{\sigma^2} = \sigma^2 \times 0.014$  for  $N=10000$ , plus a small additional factor from the covariance matrix estimation.  $1/f+wt.+ \delta$  has large noise peaks injected at 100, 1300, and 2200Hz.  $1/f+wt.+ \sim$  has the normal white and  $1/f$  features on top of which we add a sinusoidal in  $J$ , the PSD, up to 40kHz. While the HOF seems to have superior resolution in most cases, this improvement is mostly within 1  $\sigma$  uncertainty of the standard deviation, and thus assume the HOF and 32768 OF to perform equally well.

resolve those high signal-to-noise points from the zero-frequency. Clearly from table 5.4, the HOF does this just as well as the full 32768 point OF.

## 5.7 Time Offset Resolution

Whereas the amplitude estimate substantially improves by measuring the lowest frequencies of the template, signal, and noise, a time offset estimation using a 1.64ms trace (1024 points) is nearly as good as using the full 52.4288ms trace. It's not surprising that high frequencies are more important in the time offset estimation than the amplitude estimation, and this additional weight is expressed in the extra factor of  $f^2$  the time offset expected resolution:

$$\sigma_{t_0, EX}^2 = \left[ \hat{a}^2 \sum_{n=-\frac{N}{2}}^{\frac{N}{2}-1} (2\pi f_n)^2 \frac{|\tilde{A}_n|^2}{J_n} \right]^{-1}. \quad (5.18)$$

Therefore, we resort to doing a two step fit for  $\hat{t}_0$  and  $\hat{a}$ . We apply a standard 1D OF to the fast sampled data to determine  $\hat{t}_0$  (and a bad  $\hat{a}$ ), then shift our 52.4 ms time domain template of eq. 5.13 by the offset, and then determine  $\hat{a}$ .

Table 5.5 shows the slight inferiority of using 1024 points to 32768 points for the time offset fit. Also,  $\sigma_{\hat{t}_0}$  was independent of  $\hat{t}_0$  as long as the offset was within a reasonable search window ( $-100\mu\text{s}$ ,  $+100\mu\text{s}$ ), as expected. I also show that the two-stage fit does not affect the pulse amplitude estimation. For  $a = 100$ , we fit for  $\hat{a}$  first with an unknown  $t_0 = 100\mu$  and second with a known  $t_0 = 0$ , and obtain statistically equivalent resolutions. We also saw that for  $a = 20$ , as the  $t_0$  estimation deteriorates, the  $\hat{a}$  amplitude is affected no more than the 32768 point 1D OF.

## 5.8 Data Volume Consequences

In order to build the charge and phonon covariance matrix, we either require  $\sim 21000$  phonon and  $\sim 64000$  charge hybrid random noise triggers, or  $\sim 1000$  full un-averaged randoms. A new set of noise randoms will be needed per series, or at least after some amount of time over which we believe the noise is changing (we call this  $\Delta T$ ). This data volume from randoms is  $\sim 5$  times larger than the data volume projected for the true triggers during Ba and WIMP search runs.

### 5.8. Data Volume Consequences

		Noise Models		
		white (wt.)	$1/\sqrt{f} + \text{wt.}$	$1/f + \text{wt.}$
1024 point OF	$\sigma_{t_0}$ for $a = 100$	$4.9\mu\text{s}$	$3.1 \mu\text{s}$	$2.4\mu\text{s}$
	$\sigma_{t_0}$ for $a = 20$	$51\mu\text{s}$	$31\mu\text{s}$	$19\mu\text{s}$
32768 point OF	$\sigma_{t_0}$ for $a = 100$	$4.4\mu\text{s}$	$2.6 \mu\text{s}$	$2.1\mu\text{s}$
	$\sigma_{t_0}$ for $a = 20$	$49\mu\text{s}$	$25\mu\text{s}$	$16\mu\text{s}$
3008 point HOF	$\sigma_{a=100}^2$ w. t offset	9.2	9.2	9.0
	$\sigma_{a=100}^2$ w.o. t offset	9.1	9.2	8.9

Table 5.5: Time offset resolution results and the time offset’s effect on the pulse amplitude estimation. The time offset estimation with 1024 points is nearly as good as with 32768 points.

In table 5.6, we copy the projected data values from the trigger task force report, and include the additional data contribution needed for computing the HOF [43].

For the un-averaged randoms read out, the full size per year is given by:

$$\frac{M}{\Delta T} \times 76 \frac{\text{MB}}{\text{event}} \times 3.15 \times 10^7 \frac{\text{sec}}{\text{year}} \times 0.835 \quad (5.19)$$

where we have used  $M = 1000$  and  $\Delta T=3$  hours for the table ( $\frac{1000}{3\text{hr.}} \approx 0.1$  Hz). The 76MB/event comes from 12 full phonon waveforms ( $\sim 64\text{kB}$  each) and 4 full charge waveforms ( $\sim 262\text{kB}$  each), so 1.8MB per detector, multiplied by 42 detectors.

The numbers here are conservative, and there are a number of ways to improve the final data volume. It is possible that  $M = 500$  is sufficient to build  $\tilde{\mathbf{V}}^\beta$ . It’s also possible that  $\Delta T$  can be greater than 3 hours. Additionally, a noise monitor could be implemented to gauge changes in the noise, which could use a smaller rate of randoms, but could trigger a full recomputation of  $\mathbf{V}$  if need be. This could be a job for the L3 trigger. Last, some of the un-averaged randoms could be used to compute  $\tilde{\mathbf{V}}^\beta$  but never written to disk.

We also include data throughput values for the brute force computation

## 5.9. Conclusion

Mode	Rate	Event Size MB $\times$ # det.	Max Rate	Live Fraction	Ave. Rate
Ba	210 Hz	0.14 MB (0.14MB $\times$ 1)	29 MB/s	0.035	0.6 TB/wk 32 TB/year
WIMP search	0.03 Hz	5.88 MB (0.14MB $\times$ 42)	0.15MB/s	0.8	0.07 TB/wk 3.9 TB/year
error prop. $\mathbf{V}$	0.1 Hz	76MB (1.8MB $\times$ 42)	7.6MB/s	0.835	200 TB/year
brute force $\mathbf{V}$	5.9 Hz	5.88 (0.14MB $\times$ 42)	34MB/s	0.835	897 TB/year

Table 5.6: Projected data throughput values for 42 iZIPs. A 5Hz trigger rate per detector is assumed for the Ba calibration. The live fraction is the assumed fraction of operation time spent in the specified mode. The 200TB/year and 897 TB/year values assume recomputation of the covariance matrix every 3 hours (potentially naïve).

of  $\mathbf{V}$  and assume reading out  $d \times 7$  hybrid randoms. Since  $d = 9172$  for the charge  $\mathbf{V}$ , we use  $M = 64000$  per  $\Delta T$ , even though  $M = 21000$  would be sufficient for the phonon  $\mathbf{V}$ . While we win by a factor of 13 in event size, we lose by a factor of 60 in the required rate. The 5.9Hz event rate is clearly unreasonably high—with 52ms traces, this would mean reading out  $\sim 300$ ms of data for every 1s of real time.

Unless the  $M \approx d \times 7$  requirement can be improved, full readout of the randoms is clearly superior.

## 5.9 Conclusion

I introduce a method for optimal filtering the hybrid sampled waveforms proposed for SNOLAB data acquisition. I show that the pulse amplitude estimation performance of our hybrid optimal filter is just as good as a 1D optimal filter with the full non-averaged waveform.

My method does require a matrix inversion, and it computes a single optimal filter amplitude estimate in  $O(N)$  operations; it is similar in efficiency to the currently implemented non-stationary OF.

Power aliasing, due to the averaging process, introduces off diagonal elements in the frequency domain covariance matrix, which eliminates the

## 5.9. Conclusion

---

convenience of that domain that existed for 1D OFs. We therefore recommend determining the covariance matrix and evaluating  $\chi^2(\hat{a})$  in the time domain. Reliably computing the covariance matrix and its inverse is the most challenging step of the process, where either  $\sim d \times 7$  hybrid noise traces or 500 un-averaged noise traces are required (where  $d$  is the dimension of the covariance matrix). We recommend the latter from a data throughput and efficiency standpoint.

Last, these findings lead to a  $\sim \times 6.5$  increase in our projected data volume, from  $\sim 36$  TB/yr to  $\sim 236$  TB/yr (see section 5.8), but this increase seems manageable.

# Bibliography

- [1] J. H. Oort, *Proceedings of the National Academy of Science*, **10**, pp.256-260, 1924
- [2] F. Zwicky, *Astrophys. J.*, **6**, pp.110-127, 1933
- [3] V. Rubin et al., *Astrophys. J.* **225**, 107, 1978.
- [4] Y. Sofue and V. Rubin, *Ann. Rev. Astron. Astrophys.* **39**, 137, 200. arXiv:0010594 [astro-ph].
- [5] J.-P. Kneib, R. S. Ellis, I. Smail, W. J. Couch, and R. M. Sharples, *Astrophys. J.* **471**, 643, 1996, arXiv:9511015 [astro-ph]
- [6] A. Vikhlinin et al., *Astrophys. J.* **692**, 1033, 2009. arXiv:0805.2207 [astro-ph].
- [7] A. Vikhlinin et al., *Astrophys. J.* **628**, 655, 2005. arXiv:0412306 [astro-ph].
- [8] CHANDRA X-ray Observatory/NASA, <http://chandra.harvard.edu>, (accessed Aug. 15, 2015).
- [9] M. Markevitch. arXiv:0511345 [astro-ph].
- [10] C. Alcock et al., *Astrophys. J.* **550**, L169, 2001.
- [11] Planck Collaboration, arXiv:1303.5076 [astro-ph].
- [12] Planck Collaboration. *Astronomy & Astrophysics*, **571**, 2014.
- [13] S. Dodelson, *Modern Cosmology*. San Diego, CA: Academic, 2003. Print.
- [14] S. D. M. White et al., *Astrophys. J.* **209**, 27, 1984.
- [15] S. Weinberg. *Physical Review Letters* **40**, 223, 1978.
- [16] S.J. Asztalos et al., *Physical Review D.* **74**, 12006, 2006.

## Bibliography

---

- [17] E. Kolb and M. Turner, *The Early Universe*. Westview Press, 1994.
- [18] K. Griest, *Annals of the New York Academy of Sciences*, **688**, pp.390-407, 1993.
- [19] M. Kamionkowski. *High Energy Physics and Cosmology Conference*, WIMP and Axion Dark Matter, 1997.
- [20] P. J. Fox et al., *Physical Review D* **85**, 56011, 2012.
- [21] A. Geringer-Sameth et al., arXiv:1503.02320 [astro-ph]
- [22] IceCube Collaboration. arXiv:1405.5303 [astro-ph]
- [23] M. W. Goodman and E. Witten. *Physical Review D* **31**, 3059, 1985.
- [24] S. Hertel, *Advancing the Search for Dark Matter: from CDMS II to SuperCDMS*, Ph.D. Thesis, Department of Physics, Massachusetts Institute of Technology, 2012.
- [25] S. K. Lee, M. Lisanti, A. H. G. Peter, B. R. Safdi, *Phys. Rev. Lett.* **112**, 011301 (2014)
- [26] D. Moore. *A Search for Low-Mass Dark Matter with the Cryogenic Dark Matter Search and the Development of Highly Multiplexed Phonon-Mediated Particle Detectors*, Ph.D. Thesis, Division of Physics, Mathematics and Astronomy, California Institute of Technology, 2012.
- [27] R. Bernabei et al., *Journal of Physics: Conference Series* **375**, 012002, 2012.
- [28] G. F. Knoll, *Radiation Detection and Measurement* (2nd Edition). New York: John Wiley and Sons, 1989.
- [29] SuperCDMS collaboration public website, <http://cdms.berkeley.edu/gallery.html>, (accessed Aug. 15, 2015).
- [30] B. Cabrera, *Oblique propagation*, Presented at CDMS Detector Monte Carlo Workshop, 2009.
- [31] J. Lindhard et al., *Math. Fys. Medd*, **33** and **36**, (10 and 36), 1963 and 1968.
- [32] K. Irwin and G. Hilton, *Topics in Applied Physics*, **99** 2005.<http://www.springerlink.com.ezproxy.stanford.edu/content/2chgqa70h5yd1pw5/>, (accessed Aug. 15, 2015).

- [33] D. Brandt, M. Asai, P.L. Brink, B. Cabrera, E. do Couto e Silva, M. Kelsey, S.W. Leman, K. McCarthy, R. Resch, D. Wright, E. Figueroa-Feliciano, *J. Low Temp. Phys.* **167**, 485, (2013).
- [34] R. Agnese et al. arXiv: 1305.2405, 2012.
- [35] The MIDAS Data Acquisition System. <https://midas.triumf.ca/MidasWiki/index.php/MainPage> (accessed Aug. 15, 2015).
- [36] R. Brun and F. Rademakers, *Nuclear Instruments and Methods A: Accelerators, Spectrometers, Detectors and Associated Equipment* **389**, pp.81-86 1997.
- [37] J. Filippini, *A Search for WIMP Dark Matter Using the First Five-Tower Run of the Cryogenic Dark Matter Search*, Ph.D. Thesis, Department of Physics, University of California, Berkeley, 2008. <http://cdms.berkeley.edu/Dissertations/> (accessed Aug. 15, 2015)
- [38] W. H. Press, S. A. Teukolsky, W. T. Vetterling, and B. P. Flannery. *Numerical Recipes in C++*. Cambridge: Cambridge U Pr., 1992
- [39] Dutt, A., Rokhlin, V., *Fast Fourier transforms for nonequispaced data*, *SIAM J. Sci. Comput.* 14 (1993), pp. 1368-1393
- [40] Greengard, L., Lee, June-Yub., *SIAM Review*, **46**, 3, pp.443-454, 2004. <http://www.cims.nyu.edu/cmcl/nufft/nufft.html> (accessed Apr. 21, 2015).
- [41] O. Ledoit and M.Wolf, *Journal of Multivariate Analysis* **88**, pp.365-411, 2004.
- [42] J D. Scargle, *Ap.J.* **263**, pp. 835-853, 1982.
- [43] SuperCDMS SNOLAB Trigger Task Force report. November 17, 2014. Internal CDMS document link: <https://confluence.slac.stanford.edu/display/CDMS/SuperCDMS-SNOLAB+Trigger+Task+Force>(accessed Aug. 4, 2015).
- [44] Thakur, R. B., *Notes on Optimal Filter Theory* 2010. Internal CDMS document link: [http://cdms.berkeley.edu/wiki/lib/exe/fetch.php?media=software:cdmsbats\\_batroot\\_user\\_guide:ofnotes\\_nsofedit.pdf](http://cdms.berkeley.edu/wiki/lib/exe/fetch.php?media=software:cdmsbats_batroot_user_guide:ofnotes_nsofedit.pdf)(accessed June. 2, 2015).

## Appendix A

# The Imaginary Component of Zero and Nyquist Frequency

Here we prove that the imaginary component of the zero frequency and Nyquist frequency must be zero for uniformly and hybrid sampled traces.

There is a symmetry in the DFT coefficients about the zero frequency for uniformly sampled real time domain points:

$$\tilde{g}_n = \tilde{g}_{-n}^*. \quad (\text{A.1})$$

Explicitly,

$n$	$-N/2$	$-N/2 + 1$	$\dots$	$-1$	$0$	$1$	$2$	$\dots$	$N/2 - 1$
$\text{Re}(\tilde{g}_n)$	$r_{N/2}$	$r_{N/2-1}$	$\dots$	$r_1$	$r_0$	$r_1$	$r_2$	$\dots$	$r_{N/2-1}$
$\text{Im}(\tilde{g}_n)$	$0$	$-i_{N/2-1}$	$\dots$	$-i_1$	$0$	$i_1$	$i_2$	$\dots$	$i_{N/2-1}$

where the boxed quantities are overdetermined due to the symmetry. Notice that  $\tilde{g}_0 = \tilde{g}_0^*$  requires that  $\text{Im}(\tilde{g}_0) = 0$ . Said differently,  $\text{Im}(\tilde{g}_0) = 0$  because  $\tilde{g}_0$  is the average of the time domain trace, and because our trace components  $g_k$  are real, the imaginary part of the average of  $g_k$  components is zero.

$\text{Im}(\tilde{g}_{-N/2}) = 0$  for a separate reason that is related to aliasing. For frequencies exceeding the Nyquist frequency but not exceeding twice the Nyquist frequency ( $N/2 < n \leq N$ ), it can be shown that

$$\tilde{g}_n = \tilde{g}_{N-n}^*, \quad (\text{A.2})$$

(proof in Appendix B) and therefore  $\tilde{g}_{N/2} = \tilde{g}_{N/2}^*$ , giving  $\text{Im}(\tilde{g}_{-N/2}) = 0$ .

Note that the proof of eq. A.2 depends on uniformly sampled data. It therefore doesn't hold, in general, for the hybrid Fourier coefficients. However, because only the fast sampled data has any sensitivity to the Nyquist

*Appendix A. The Imaginary Component of Zero and Nyquist Frequency*

---

Fourier coefficient, and the fast sampled data is uniformly sampled, the symmetry holds for the Nyquist Fourier coefficient of the hybrid traces.

## Appendix B

# Derivation of Aliasing Frequencies

The standard DFT of an  $N$  point time domain trace,  $g$ , sampled at rate  $R$  and spanning time  $T$  is given by:

$$\tilde{g}_n = \frac{1}{N} \sum_{k=-\frac{N}{2}}^{\frac{N}{2}-1} g_k e^{-2\pi i f_n t_k} \quad (\text{B.1})$$

where  $\tilde{g}_n$  is evaluated for  $n = -\frac{N}{2} \rightarrow \frac{N}{2} - 1$  in integer steps,  $f_n = \frac{n}{T}$ , and  $t_k = \frac{k}{R}$ . Therefore the Nyquist frequency,  $f_{Nyq} = R/2$ , corresponds to  $n = \frac{TR}{2} = \frac{N}{2}$ .

In order to derive which frequencies above  $f_{Nyq}$  alias to a single frequency below  $f_{Nyq}$ , we calculate the DFT of a time domain trace composed of a single frequency greater than the Nyquist,  $f_{GN}$ . The time domain trace, with amplitude 1, is:

$$g_k = \exp[2\pi i f_{GN} t_k] \quad (\text{B.2})$$

and we define

$$f_{GN} = \frac{1}{T} \left[ \frac{N}{2} + m \right], \quad (\text{B.3})$$

so our signal's frequency exceeds the Nyquist frequency by  $\frac{m}{T}$ . The DFT of this trace becomes:

$$\tilde{g}_n = \frac{1}{N} \sum_{k=-\frac{N}{2}}^{\frac{N}{2}-1} \exp[-2\pi i t_k (f_n - f_{GN})] \quad (\text{B.4})$$

$$\tilde{g}_n = \frac{1}{N} \sum_{k=-\frac{N}{2}}^{\frac{N}{2}-1} \exp[-2\pi i \frac{k}{N} (n - \frac{N}{2} - m)]$$

Notice that if the argument of the exponential is equal to an integer multiple of  $2\pi$ , that is:

$$\tilde{g}_n = \frac{1}{N} \sum_{k=-\frac{N}{2}}^{\frac{N}{2}-1} \exp[-2\pi iz]$$

where  $z \in \mathbf{Z}$ , each element of the sum equals  $1+0i$  and they add coherently.<sup>5</sup> Without coherent adding, each term will be between -1 and 1, and the sum will average to  $\sim 0$ .

Therefore  $\frac{k}{N}(n - \frac{N}{2} - m) = z$  is the condition for the signal to alias to the  $\tilde{g}_n$  coefficient, which boils down to  $(n - \frac{N}{2} - m)/N = z$  because  $k$  is an integer. Solving for  $m$  and plugging back in for  $f_{GN}$  gives the frequencies that alias to  $\frac{n}{T}$ :

$$f_{GN} = \frac{1}{T} [-Nz + n]. \quad (\text{B.5})$$

As an example, the frequencies that alias to  $\frac{N}{6T}$  are:

$$\dots, \frac{-11 N}{6 T}, \frac{-5 N}{6 T}, \frac{7 N}{6 T}, \frac{13 N}{6 T}, \dots$$

and recalling the symmetry of Fourier coefficient about the zero frequency for real traces,<sup>6</sup>

$$\tilde{g}_n = \tilde{g}_{-n}^*$$

the complete list of aliased frequencies is:

$$\dots, \frac{-13 N}{6 T}, \frac{-11 N}{6 T}, \frac{-7 N}{6 T}, \frac{-5 N}{6 T}, \frac{5 N}{6 T}, \frac{7 N}{6 T}, \frac{11 N}{6 T}, \frac{13 N}{6 T}, \dots$$

All frequencies that alias to  $\frac{n}{T}$  can therefore be expressed concisely as:

$$f_{\text{alias}} = z \frac{N}{T} \pm \frac{n}{T}. \quad (\text{B.6})$$

Using eq. , we compute the  $f_{\text{alias}}$  values as they correspond to fig. 5.4. We are examining aliasing below the slow sampled Nyquist frequency of hybrid phonon waveforms,  $f_{Nyq,slow} = 19531.25Hz$ , and so  $\frac{N}{T} = 39062.5Hz$ .

<sup>5</sup>notice that there is an additional proof (omitted here) for the coherent adding of the imaginary components

<sup>6</sup>it seems wrong to cite this symmetry given that we used a complex time domain trace (eq. B.2), but had we used  $g_k = \cos[2\pi i f_{GN} t_k]$  we still would have obtained eq. B.5, just with more steps.

### Appendix B. Derivation of Aliasing Frequencies

---

We are also examining aliasing to 9538Hz, so  $\frac{n}{T} = \frac{500}{52.4288\text{ms}} = 9538\text{Hz}$ . The  $f_{\text{alias}}$ , for  $z = 1 \rightarrow 8$ , are:

29524.5, 48600.5, 68587, 87663, 107649.5, 126725.5, 146712, ...

...165788, 185774.5, 204850.5, 224837, 243913, 263899.5, 282975.5, 302962

which agree with the frequencies in figure 5.4.